Substitution of Co with Ni in Co/Al_2O_3 catalysts for Fischer-Tropsch synthesis

Michela Martinelli[1], Sai Charan Karuturi[2], Richard Garcia[3], Caleb D. Watson[3], Wilson D. Shafer[4], Donald C. Cronauer[5], A. Jeremy Kropf[5], Christopher L. Marshall[5], and Gary Jacobs[1,3*]

[1] University of Kentucky Center for Applied Energy Research, 2540 Research Park Drive, Lexington, KY 40511, USA; michela.martinelli@uky.edu
[2] Department of Mechanical Engineering, University of Texas at San Antonio, One UTSA Circle, San Antonio, TX 78249, USA; saicharan.karuturi@utsa.edu, gary.jacobs@utsa.edu
[3] Department of Biomedical Engineering and Chemical Engineering, University of Texas at San Antonio, One UTSA Circle, San Antonio, TX 78249, USA; g123richard@gmail.com, saicharan.karuturi@utsa.edu, gary.jacobs@utsa.edu
[4] Asbury University, One Macklem Drive, Wilmore, KY 40390, USA; wilson.shafer@asbury.edu
[5] Argonne National Laboratory, Argonne, IL 60439, USA; dccronauer@anl.gov, kropf@anl.gov, marshall@anl.gov
* Correspondence: gary.jacobs@utsa.edu; +1-210-458-7080 (G.J.)

Abstract: The effect of cobalt substitution with nickel was investigated for the Fischer-Tropsch synthesis reaction. Catalysts having different Ni/Co ratios were prepared by aqueous incipient wetness co-impregnation, characterized and tested using a continuously stirrer tank reactor (CSTR) for more than 200 h. The addition of nickel did not significantly modify the morphological properties measured. XRD, STEM and TPR-XANES results showed intimate contact between nickel and cobalt, strongly suggesting the formation of a Co-Ni solid oxide solution in each case. Moreover, TPR-XANES indicated that nickel addition improves the cobalt reducibility. This may be due to H_2 dissociation and spillover, but more likely due to a chemical effect of intimate contact between Co and Ni resulting in Co-Ni alloying after activation. FTS testing revealed a lower initial activity when nickel was added. However, CO conversion was observed to continuously increase with time on-stream until a steady-state value (34-37% depending on Ni/Co ratio) was achieved, which was very close to the value observed for undoped Co/Al_2O_3. This trend suggests nickel can stabilize cobalt nanoparticles even if at a lower weight % of Co. Currently, the cobalt price is 2.13 times the price of nickel. Thus, comparing the activity/$, the catalyst with a Ni/Co ratio of 25/75 has better performance than the unpromoted catalyst. Finally, nickel promoted catalysts exhibited slightly higher initial selectivity to light hydrocarbons initially, but this difference typically diminished with time on-stream; once leveling off in conversion was achieved, the C_5+ selectivities were similar (~80%) for Ni/Co ratios up to 10/90, and only slightly lower (~77%) at Ni/Co of 25/75.

Keywords: Fischer-Tropsch synthesis, bimetallic catalyst, cobalt-nickel alloys, TPR-XANES/EXAFS

1. Introduction

Fischer-Tropsch synthesis (FTS) is a catalytic reaction which converts syngas, a mixture of CO and H_2 derived from natural gas, coal, and/or biomass, to high quality fuels. The active metals for FTS are iron, cobalt, nickel and ruthenium. Among these metals, ruthenium is the most active. However, its application for large-scale FTS plants is impractical because of low abundance and very high cost [1]. In contrast, nickel is cheaper, but high selectivities to short-chained hydrocarbons, especially methane, are obtained because of its high hydrogenation capability [2]. Thus, cobalt and iron are the only relevant catalysts which are currently used commercially. Cobalt is especially advantageous for converting methane derived syngas because of its high activity and selectivity to linear long-chained hydrocarbons, low deactivation rate and finally low activity for water-gas shift

(WGS) [3, 4]. However, cobalt is more expensive than iron. Indeed, the cobalt price range in the last five years has been in the range of 22-100 $/kg [5].

The activity of cobalt catalysts depends on the number of exposed Co^0, the active sites, on the catalyst surface [6]. Systems with relatively high dispersions are needed in order to maximize the surface availability of Co^0. For this reason, cobalt is typically supported on high surface area carriers with strong interactions (e.g., Al_2O_3, TiO_2). However, thermodynamic studies suggest cobalt nanoparticles lower than 4 nm might be re-oxidized by water under FTS reaction conditions [7, 8]. Thus, the optimal particle sizes are in the range of 6-10 nm [9]. Even if the particle size, as well as the interaction with the support, are optimized, the majority of the cobalt is locked within the particle instead of being exposed to the surface. Therefore, the incorporation of a second metal, less expensive and with similar electronic properties of cobalt, could be a possible route to decrease the total preparation cost of the catalyst. DFT screening was used by Van Helden et al. [10] to identify the alloys which have similar adsorption and electronic properties to cobalt catalyst. $NiCo_3$, $AlNi_3$ and $SiFe_3$ are suitable cheaper candidates. However, $SiFe_3$ and $AlNi_3$ are quite difficult to produce at the nanoscale level. In contrast, Co-Ni alloys can be easily prepared at different Ni/Co ratios. Ni-Mn bimetallic systems were also investigated during CO_x hydrogenation. The authors reported the formation of $NiMnO_3$ when Ni/Mm ratio is higher than 1 and higher activity for CO hydrogenation [11].

Cobalt and nickel have different electronic configurations. Cobalt is a d^7 metal which dissociates CO and stabilizes the vinylic intermediate. This intermediate species is stable in an sp^3 configuration which favors the chain growth to linear hydrocarbons during FTS [2]. In contrast, nickel (d^8 metal) has a greater electronic back-donation capability. Thus, vinylic intermediates cannot be sufficiently stabilized, thus favoring the production of light saturated hydrocarbons, especially methane. Therefore, it is of fundamental importance to investigate alloys with different Ni/Co ratios in order to determine the optimal nickel loading for (1) the stability of the vinylic intermediate, (2) catalyst stability with time on-stream, and (3) high selectivity to longer chained hydrocarbons.

Co-Ni alloys for FTS were investigated by different authors [10, 12-22]. Ishihara et al. studied Co-Ni alloys supported on $MnO-ZrO_2$ [13] and SiO_2 [12, 14]. The authors found that the electronic interactions between nickel and cobalt create new adsorption sites, which strengthens the adsorption of hydrogen and enhances the catalytic activity. Further research has suggested that nickel facilitates reduction of cobalt, shifting it to lower temperature, as well as increasing the cobalt dispersion [16, 18]. Moreover, Rytter et al. [18] observed that cobalt catalyst with nickel loadings up to 5 wt% have an improved stability because of the suppression of coking through nickel decoration of the cobalt surface. Recently, Lòpez-Tinoco et al. [20] characterized well-controlled nanoparticles consisting of Co-Ni alloys and compared them with a conventional heterogenous catalyst. TPR-XANES/EXAFS showed that cobalt and nickel have an oxidation state which can be tuned from +2 to 80% metallic. However, well-controlled nanoparticles can currently be prepared in only small amounts, and as such, cannot be easily used for commercial FTS applications. The authors prepared a conventional nickel-cobalt catalyst and found similar activity to Co/Al_2O_3 at steady-state conditions. However, additional investigations are needed in order to speculate the role of nickel in these bimetallic systems.

In the present work, catalysts with different Ni/Co ratios were prepared and characterized by BET, XRD, ICP, TPR-XANES, and STEM. The activity and the catalytic stability have been evaluated by testing the catalyst in a CSTR reactor for more than 200 h.

2. Results

2.1 Catalyst characterization

BET surface areas for the prepared catalysts are shown in Table 1. The surface area, pore volume and pore diameter are similar among all the samples suggesting the substitution of cobalt with nickel does not affect the morphological properties. Table 1 also shows the ICP results. The cobalt loading

is slightly higher (~30%) than the theoretical value (25%), whereas all Ni/Co ratios are consistent with the nominal values.

XRD patterns for Al_2O_3 and the oxide catalysts are plotted in Figure 1. All the catalysts show the characteristic reflection peaks associated with Co_3O_4 (i.e. $2\Theta = 36.8°$). No diffraction peaks correlated to nickel compounds are detected for the nickel promoted catalyst. This suggests nickel is well dispersed, as well as the formation of a Co-Ni solid oxide solution.

Table 1: BET, BJH and ICP results for the prepared catalysts.

Sample ID	A_s (BET) [m^2/g]	V_p (BJH Des) [cm^3/g]	D_p (BJH Des) [Å]	%Co	%Ni
25%Co	95.5	0.243	93	30.21	-
25%M – 5%Ni-95%Co	92.9	0.226	91	30.49	1.43
25%M – 10%Ni-90%Co	96.5	0.227	94	31.58	2.97
25%M – 25%Ni-75%Co	96.0	0.236	89	24.86	7.7
25%M – 50%Ni-50%Co	91.6	0.237	87	17.4	16.2

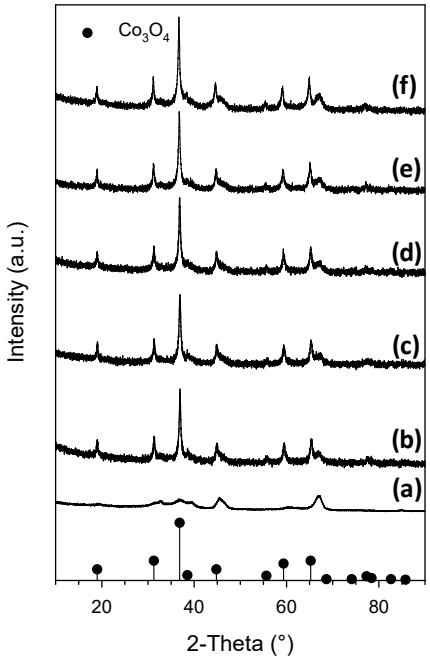

Figure 1: XRD for (a) 25%Co/Al_2O_3, (b) 25%M (M = 5%Ni-95%Co)/Al_2O_3, (c) 25%M (M = 10%Ni-90%Co)/Al_2O_3, (d) 25%M (M = 25%Ni-75%Co)/Al_2O_3, and (e) 25%M (M = 50%Ni-50%Co)/Al_2O_3.

Figure 2 shows TEM and STEM of reduced 25%M (10%Ni-90%Co)/Al_2O_3. The particle sizes are distributed between 18 and 23 nm, whereas the presence of nickel and cobalt was confirmed by EDS analysis. These two metals are uniformly distributed confirming the formation of a Ni-Co solid oxide solution as pointed it out from XRD. The Co/Ni weight ratio is close to 10, similar to the theoretical value. The particle sizes for the 25%Co/Al_2O_3 are between 15 and 20 nm (Figure 3). EDS analysis shows areas richer in cobalt (until 55 wt. %), and others poorer in cobalt (10 wt. %); however, the average cobalt loading is close to 28 wt.% over an extended area.

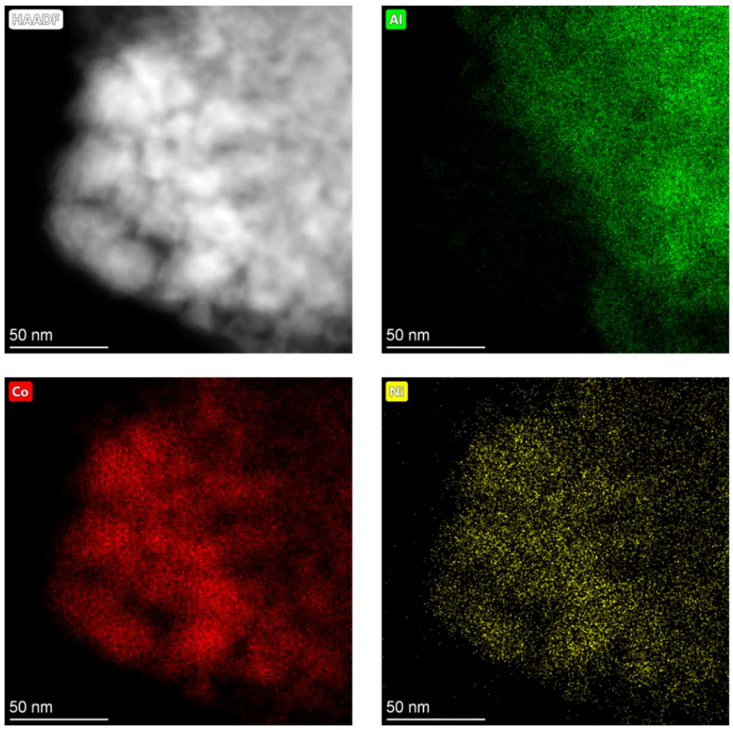

Figure 2: HAADF-STEM image of sample 25%M (10%Ni-90%Co). Elemental mapping legend: (Yellow) Nickel, (Red) Cobalt, and (Green) Aluminum.

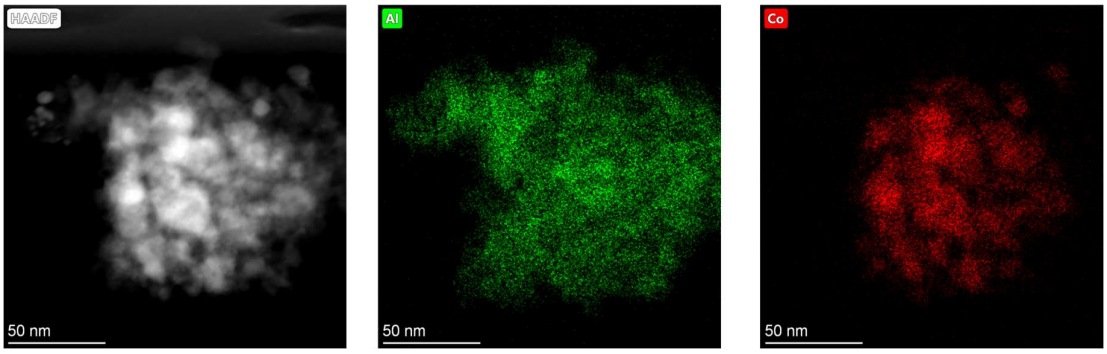

Figure 3: HAADF-STEM image of sample 25%Co. Elemental mapping legend: (Green) Aluminum, and (Red) Cobalt.

Hydrogen chemisorption with pulse reoxidation results are presented in Table 2. The degree of reduction results are similar with those of the TPR-XANES/EXAFS data as it will be shown in the next sections. With increasing Ni/Co ratio, the mixed metal oxides exhibit more facile reduction. There also appears to be a slight increase in average metal diameter with increases in Ni/Co ratio as well. If the traditional approach, designated method #1, of assuming complete oxidation of reduced metals to their respective oxides is used, then the increase is only slight (i.e., from 11.2 to 15.2 nm). However, if method #2 is used, the difference is wider (i.e., from 7.0 to 13.5 nm). Method #2 assumes that, during reduction, all Co_3O_4 reduces to CoO, while only a portion of CoO reduces to Co^0 (and a fraction of NiO reduces to Ni^0). Thus, during the reoxidation with O_2 pulse, the Ni^0 and Co^0 oxidize to NiO and CoO, and all CoO (including CoO obtained from Co^0 oxidation as well as the CoO previously resulting from merely partial reduction of Co_3O_4) oxidizes to Co_3O_4.

Table 2: H_2 chemisorption and pulse O_2 titration.

μmol H_2 desorbed/g_{cat}	Uncorr. % Disp.	Uncorr. Diam. (nm)	O_2 uptake (μmol/g_{cat})	* % Red.	** % Red.	* Corr. % Disp.	** Corr. % Disp.	* Corr. Diam. (nm)	** Corr. Diam. (nm)
25%Co/Al_2O_3									
91.3	4.3	24	1324	46.8	29.1	9.2	14.8	11.2	7.0
25%M(95%Co-5%Ni)/Al_2O_3									
104.0	4.9	21.1	1317	47.3	30.4	10.4	16.1	10.0	6.4
25%M(90%Co-10%Ni)/Al_2O_3									
92.5	4.4	24	1495	54.6	40.5	8.0	10.8	12.9	9.6
25%M(75%Co-25%Ni)/Al_2O_3									
94.6	4.5	23.2	1563	59.9	48.7	7.5	9.2	13.9	11.3
25%M(50%Co-50%Ni)/Al_2O_3									
94.7	4.5	23.1	1594	65.7	58.5	6.8	7.6	15.2	13.5

* method #1 assuming Ni^0 oxidizes to NiO and Co^0 oxidizes to Co_3O_4.

** method #2 assuming all Co_3O_4 reduced to CoO and some NiO and CoO reduced to Ni^0 and Co^0. During oxidation, then, the Ni^0 and Co^0 oxidize to NiO and CoO, and all CoO oxidizes to Co_3O_4.

2.2 Cobalt reducibility

H_2 TPR-XANES

Figures 4 and 5 display H_2 TPR-XANES spectra for the prepared samples at the Co K-edge as a function of increasing Ni/Co ratio using two different perspectives. The perspective of Figure 4 is versus temperature, whereas the perspective of Figure 5 is that of photon energy. XANES snapshots at the point of 100% Co_3O_4, 100% CoO, and the final spectrum at the point of maximum reduction to Co^0 are shown in Figure 6. Cobalt oxides reduce to metallic compounds in two steps: (I) $Co_3O_4 + H_2 = 3CoO + H_2O$ and (II) $3CoO + 3H_2 = 3Co^0 + 3H_2O$. Figure 6 shows that with increasing Ni/Co ratio, the reduction of cobalt oxides systematically moves to lower temperature.

For all of the catalysts, the initial spectrum at 25°C resembles that of Co_3O_4. The point of 50%Co_3O_4/50%CoO was reached at 339 °C (Ni/Co = 0/100), 308 °C (Ni/Co = 5/95), 294 °C (Ni/Co = 10/90), 273 °C (Ni/Co = 25/75), and 249 °C (Ni/Co = 50/50). Thus, up to a Δ 90°C decrease in reduction temperature was achieved. The point of 100%CoO was obtained at 400 °C (Ni/Co = 0/100), 330 °C (Ni/Co = 5/95), 330 °C (Ni/Co = 10/90), 305 °C (Ni/Co = 25/75), and 278 °C (Ni/Co = 50/50). Thus, up to a Δ 122°C decrease in reduction temperature was obtained in converting Co_3O_4 to CoO.

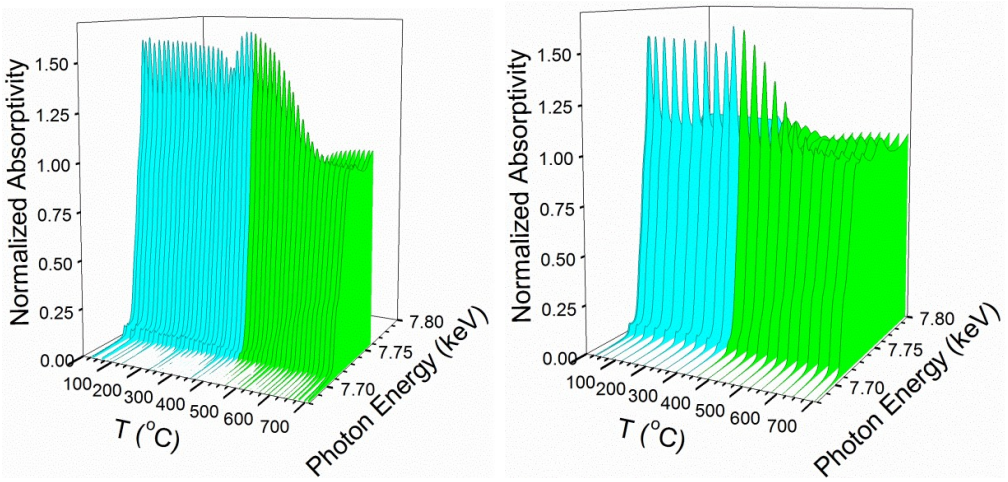

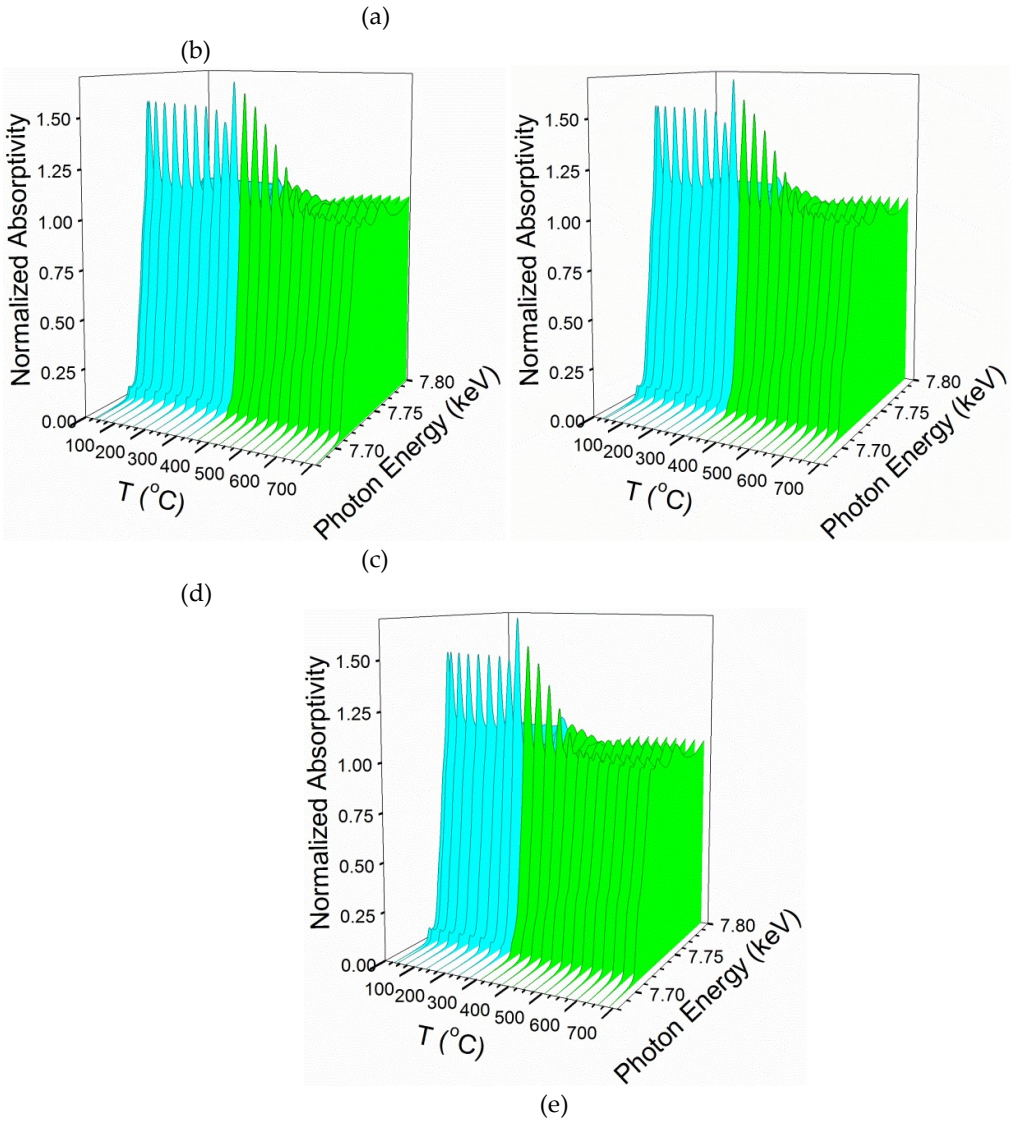

Figure 4: H_2-TPR-XANES spectra at the Co K-edge of (a) 25%Co/Al_2O_3, (b) 25%M (M = 5%Ni-95%Co)/Al_2O_3, (c) 25%M (M = 10%Ni-90%Co)/Al_2O_3, (d) 25%M (M = 25%Ni-75%Co)/Al_2O_3, and (e) 25%M (M = 50%Ni-50%Co)/Al_2O_3.

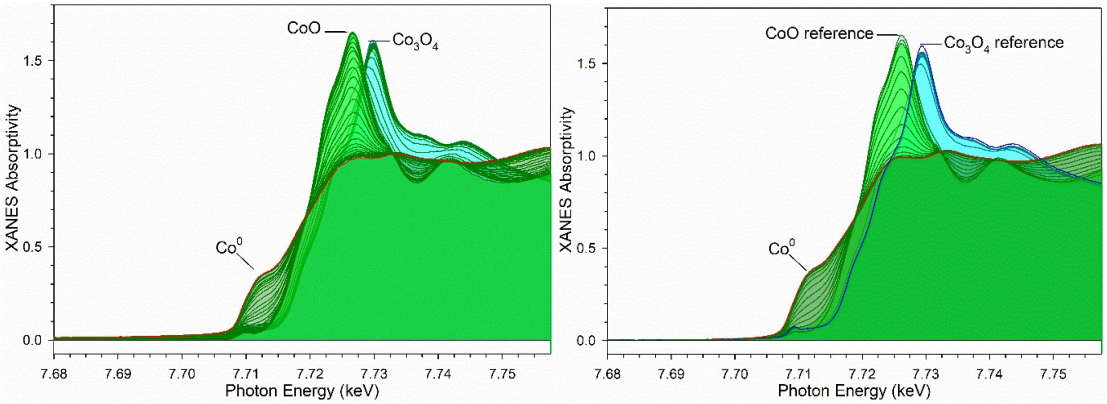

(a)

(b)

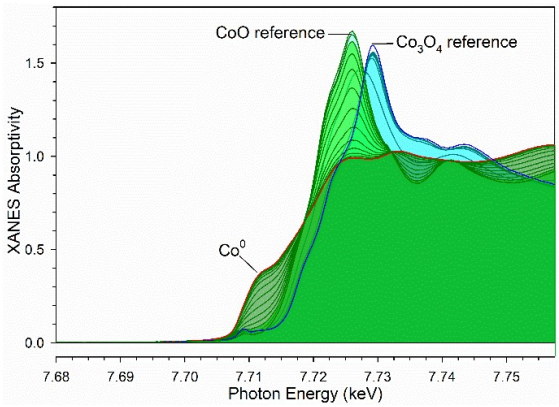

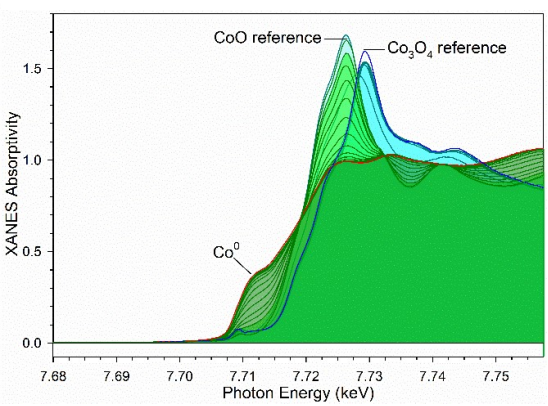

(c)

(d)

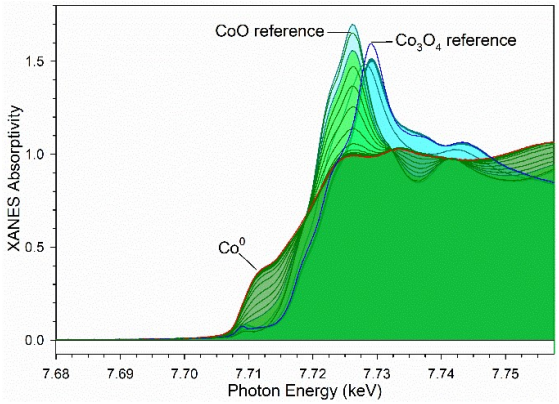

(e)

Figure 5: H_2-TPR-XANES spectra (XY view) at the Co K-edge of (a) 25%Co/Al_2O_3, (b) 25%M (M = 5%Ni-95%Co)/Al_2O_3, (c) 25%M (M = 10%Ni-90%Co)/Al_2O_3, (d) 25%M (M = 25%Ni-75%Co)/Al_2O_3, and (e) 25%M (M = 50%Ni-50%Co)/Al_2O_3.

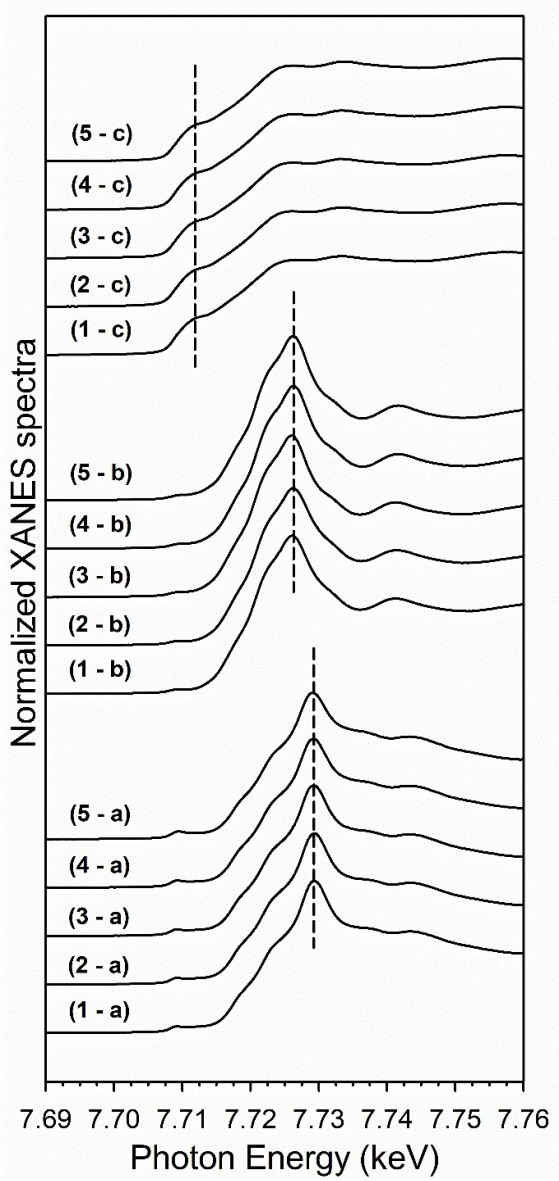

Figure 6: Co K-edge XANES spectra of (a) initial point consisting of primarily Co_3O_4, (b) point of maximum CoO content, and (c) final spectrum consisting of primarily Co^0 for (1) 25%Co/Al_2O_3, (2) 25%M (M = 5%Ni-95%Co)/Al_2O_3, (3) 25%M (M = 10%Ni-90%Co)/Al_2O_3, (4) 25%M (M = 25%Ni-75%Co)/Al_2O_3, (5) 25%M (M = 50%Ni-50%Co)/Al_2O_3.

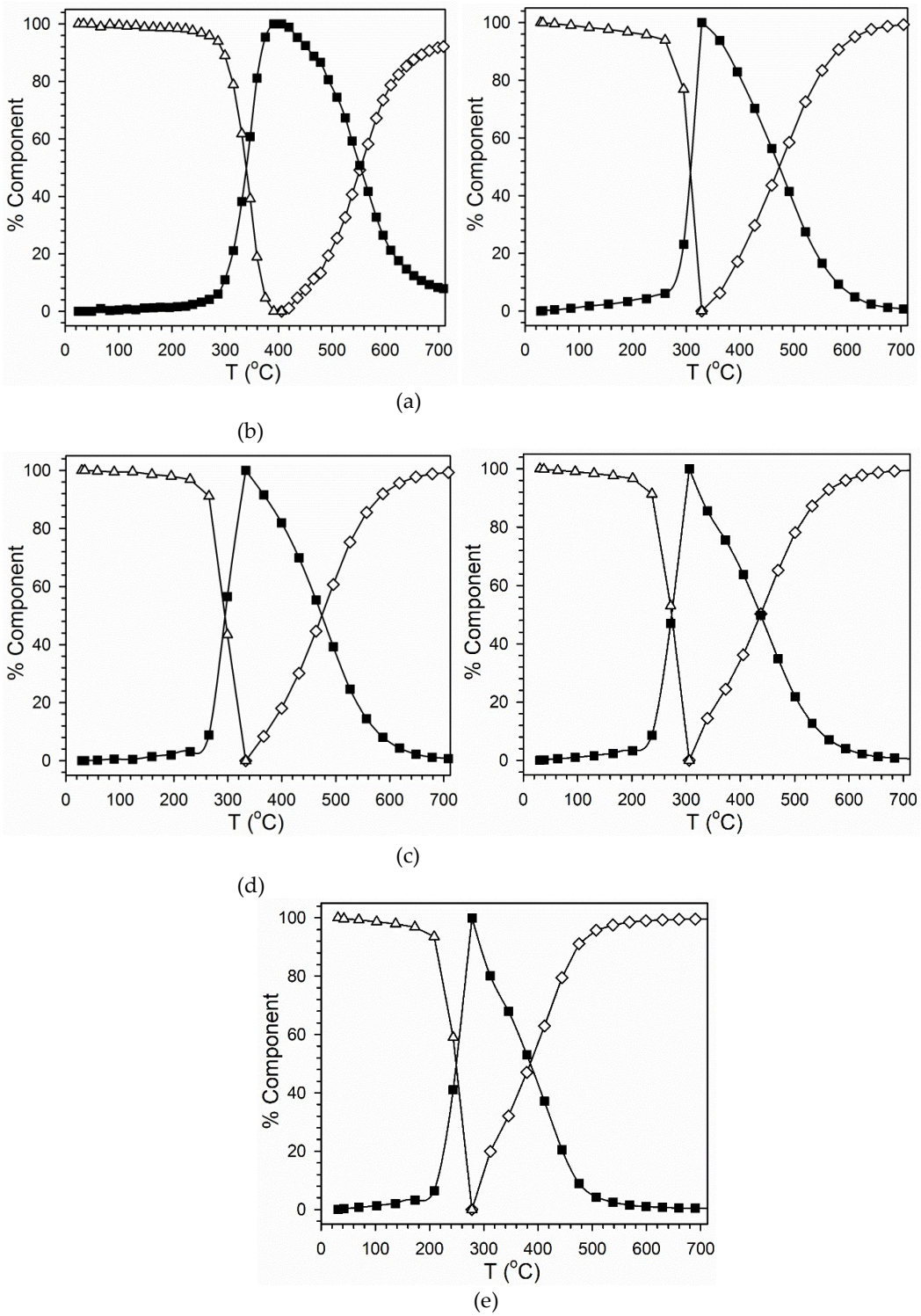

Figure 7: LC fittings of H_2-TPR-XANES spectra at the Co K-edge of (a) 25%Co/Al_2O_3, (b) 25%M (M = 5%Ni-95%Co)/Al_2O_3, (c) 25%M (M = 10%Ni-90%Co)/Al_2O_3, (d) 25%M (M = 25%Ni-75%Co)/Al_2O_3, and (e) 25%M (M = 50%Ni-50%Co)/Al_2O_3.

The point of 50%CoO/50%Co^0 was attained at 553 °C (Ni/Co = 0/100), 473 °C (Ni/Co = 5/95), 473 °C (Ni/Co = 10/90), 437 °C (Ni/Co = 25/75), and 386 °C (Ni/Co = 50/50). Thus, up to a Δ 167°C decrease in reduction temperature was achieved by doping Co with Ni. It is evident that, unlike the Group 10 metal Pt, where substantial shifts in the reduction of Co oxides were observed with minute amounts of Pt, significantly higher quantities of Ni are required to achieve the same level of reduction. For example, just 0.5%Pt was able to facilitate a decrease of 194°C for the Co_3O_4 to CoO transition, and a decrease of 120°C from CoO to Co^0 [23], which is < $1/40^{th}$ of the atomic amount. In comparison with the TPR profile of CoO during reduction of undoped 25%Co/Al_2O_3, this is likely in part due to the strong interactions between Ni oxides and alumina support.

H_2 TPR-EXAFS

TPR-EXAFS spectra at the Co K-edge are shown in Figures 8 and 9, including a plot that highlights the temperature (Figure 8), and a plot that emphasizes differences as a function of distance from the absorber (Figure 9). The initial cyan spectrum of each TPR-EXAFS profile represents Co_3O_4. It can be differentiated from CoO (i.e., the first green spectrum) by the fact that the Co-O peak is significantly more intense, while the Co-Co coordination peak is broadened due to the presence of additional oxygen atoms (Figure 9). Following the transition to CoO, the CoO slowly converts to Co^0, resulting in a final well-resolved peak for Co-Co metal coordination. In a manner similar to Pt and Ru promoters, Ni facilitates both steps of reduction – however, as mentioned previously, on an atomically equivalent basis, Ni is far less effective than either Pt or Ru [23]. It differs from Re, which only catalyzes the second step, CoO reduction to Co^0. Unlike Pt and Ru oxides, which reduce at low temperatures, Re oxide was observed to reduce at a similar range as Co_3O_4 reduction to CoO (e.g. 300 – 350°C), and it was supposed that a reduced form was necessary in order to facilitate CoO reduction through a H_2 dissociation and spillover mechanism [23]. Thus, if a hydrogen dissociation and spillover mechanism operated for the case of Ni, one would expect that NiO should reduce to Ni^0 prior to the reduction of Co oxides. Based on the Ni X-ray absorption spectroscopy results, this does not seem to be the case.

2.3 Nickel reducibility

H_2 TPR-XANES

TPR-XANES spectra in Figure 11 and 12 at the Ni K-edge reveal that, initially, Ni oxide is associated with Co_3O_4 (see spectra in cyan color) and this Ni oxide subsequently undergoes a change in electronic structure to a form of Ni oxide associated with CoO (initial green spectrum). This change is best observed by examining the head-on spectra of Figure 13, as well as the XANES snapshots shown in Figure 14. Let us refer to this transition as step one. Step two is further reduction of Ni^{2+} to Ni^0 (dark green spectra in Figure 12).

Figure 14 provides quantitative information regarding the Ni species present along the TPR trajectory. In step one, the point of 50%Ni^{2+}-Co_3O_4 / 50%Ni^{2+}-CoO was reached at 333 °C (Ni/Co = 5/95), 286 °C (Ni/Co = 10/90), 261 °C (Ni/Co = 25/75), and 234 °C (Ni/Co = 50/50). Thus, up to a Δ 99°C decrease in reduction temperature was achieved (compared to a Δ of 60°C for the cobalt system over the same range of loading), and the temperatures match well with those of the Co_3O_4 to CoO transitions described earlier at the 50% point of conversion, especially at higher Ni/Co ratios. The point of 100%Ni^{2+}-CoO was obtained at 362 °C (Ni/Co = 5/95), 332 °C (Ni/Co = 10/90), 305 °C (Ni/Co = 25/75), and 278 °C (Ni/Co = 50/50). Thus, up to a Δ 84°C decrease in reduction temperature was obtained in converting 100%Ni^{2+}-Co_3O_4 to 100%Ni^{2+}-CoO (compared to a Δ of 52°C for the cobalt system over the same range of loading). Once again, the temperatures match quite well with those of the Co_3O_4 to CoO transitions described earlier for Co K-edge data, and match nearly perfectly at Ni/Co loadings of 10%, 25%, and 50%.

Continuing, the point of 50%Ni^{2+}-CoO/50%Ni^{0} was achieved at 503 ^{o}C (Ni/Co = 5/95), 482 ^{o}C (Ni/Co = 10/90), 458 ^{o}C (Ni/Co = 25/75), and 412 ^{o}C (Ni/Co = 50/50). Thus, up to a Δ 91^{o}C decrease in reduction temperature was achieved by doping Co with Ni (compared to a Δ of 87^{o}C for the cobalt system over the same range of loading).

The similarities in temperature ranges between Co_3O_4 to CoO and the Ni^{2+}-Co_3O_4 to Ni^{2+}-CoO transitions, as well those between CoO to Co^{0} and Ni^{2+}-CoO to Ni^{0}-Co^{0} transitions, suggest that the effect may not be simply a H_2 dissociation and spillover mechanism, but rather a chemical effect due to intimate contact between Ni and Co in both oxide (e.g., solid solution) and metallic (e.g., alloy) phases, throughout the TPR trajectory.

H_2 TPR-EXAFS

Comparing the TPR-EXAFS spectra of Figure 15 with Figure 8, Figure 16 with Figure 9, and Figure 17 with Figure 10, it is remarkable how closely the behavior of Ni resembles that of Co. The initial cyan spectra of Figures 15 and 16 reveal that the first Ni-O peak is more intense than that of the green Ni-O peak, suggesting greater coordination to oxygen, while the second peak for Ni-Ni coordination in the initial cyan spectra is more broadened as compared to the initial green spectra, consistent with greater oxygen content forcing Ni atoms apart. Figure 17 highlights the differences between the local atomic structure of different species along the TPR profile (e.g., Co_3O_4 associated with Ni^{2+}; CoO associated with Ni^{2+}; and Co^{0} associated with Ni^{0}).

Figure 18 and 19, as well as Table 3, show EXAFS fittings for the Co K-edge and Ni K-edge data following TPR-EXAFS and cooling to ambient temperature. A simple model was developed previously [20] and applied here, where metal coordination to Ni (whether the core atom was Co or Ni) was given as a fraction, X, of metal-cobalt coordination. Using this approach, excellent fittings with low r-factors were obtained Co-Ni alloy formation is consistent with EXAFS fitting, but it cannot be considered a prove since Co and Ni are too closely related in size.

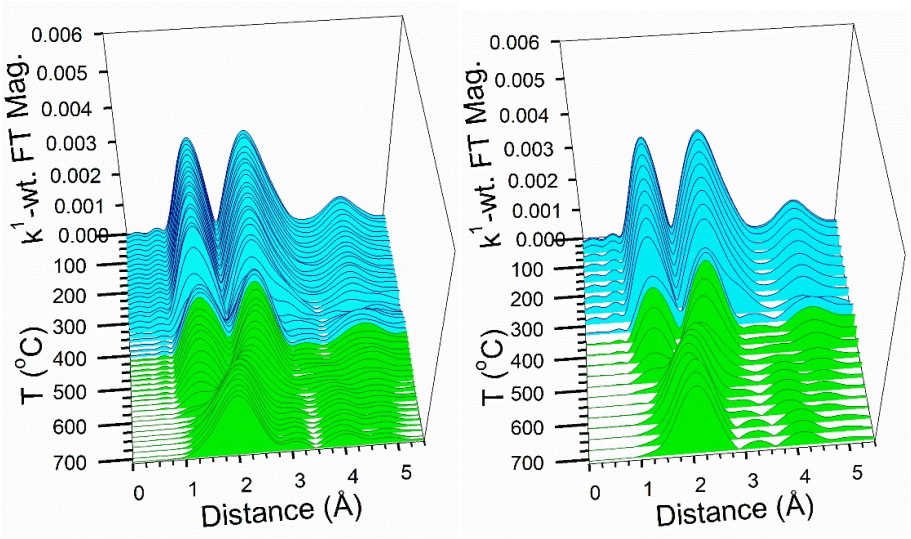
k¹-wt. FT Mag.
T (°C)
Distance (Å)

(a)

(b)

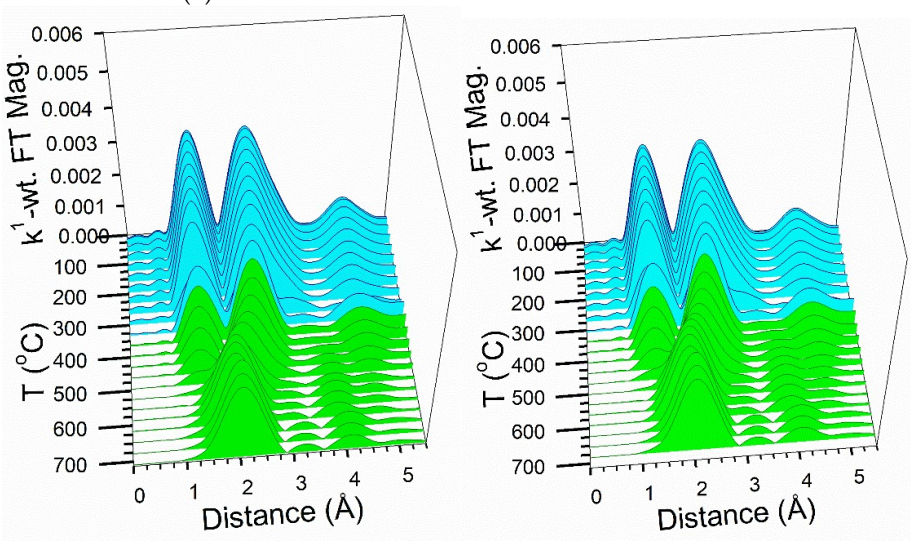
k¹-wt. FT Mag.
T (°C)
Distance (Å)

(c)

(d)

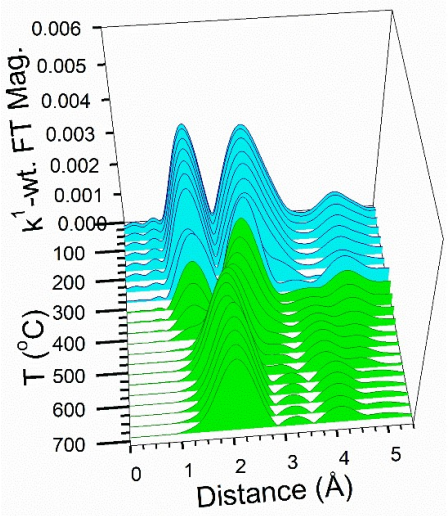
k¹-wt. FT Mag.
T (°C)
Distance (Å)

(e)

Figure 8: H_2-TPR-EXAFS spectra at the Co K-edge of (a) 25%Co/Al_2O_3, (b) 25%M (M = 5%Ni-95%Co)/Al_2O_3, (c) 25%M (M = 10%Ni-90%Co)/Al_2O_3, (d) 25%M (M = 25%Ni-75%Co)/Al_2O_3, and (e) 25%M (M = 50%Ni-50%Co)/Al_2O_3. (Cyan) is reduction of Co_3O_4 to CoO, and (Green) CoO to Co^0.

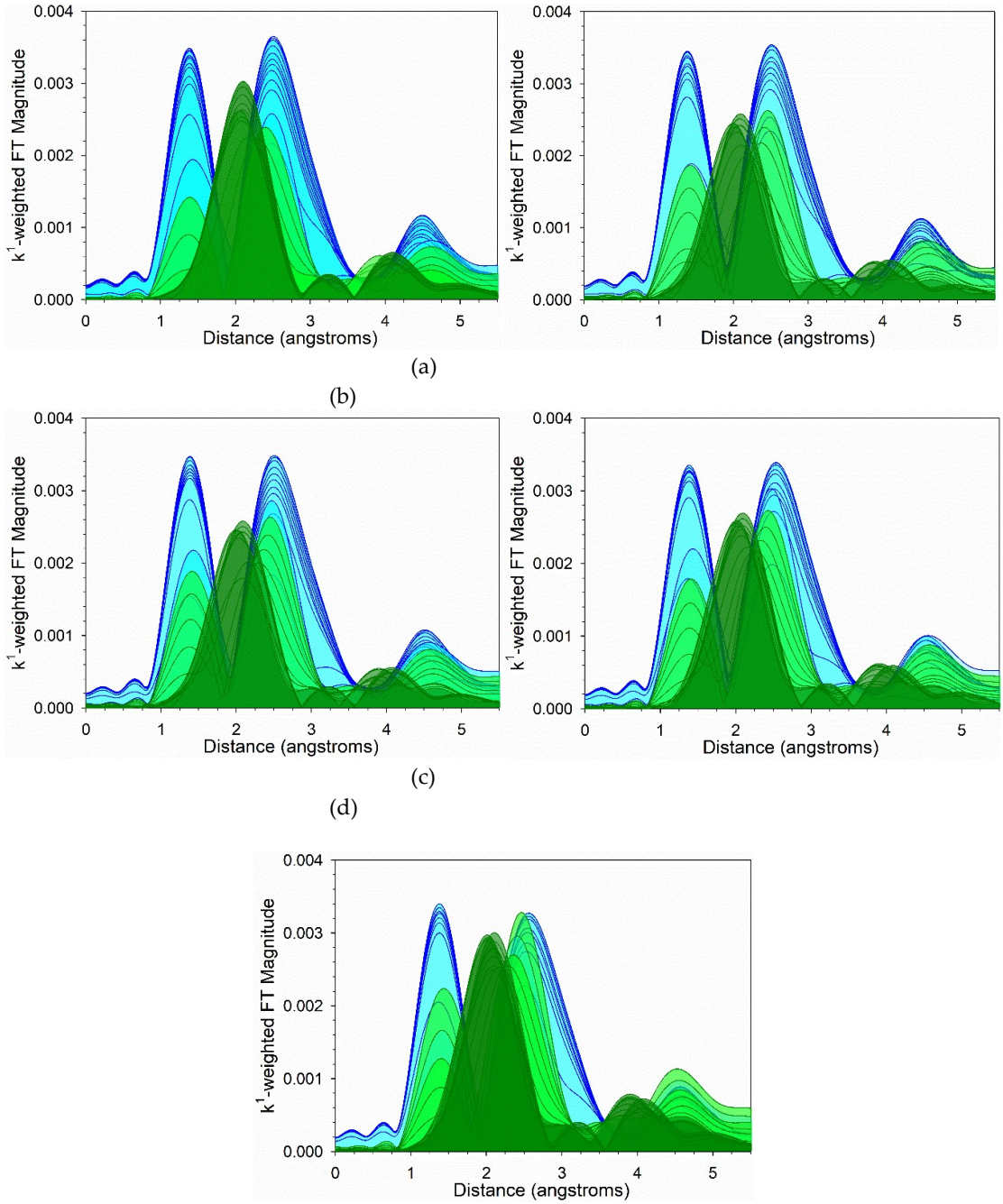

Figure 9: H_2-TPR-EXAFS spectra (XY view) at the Co K-edge of (a) 25%Co/Al_2O_3, (b) 25%M (M = 5%Ni-95%Co)/Al_2O_3, (c) 25%M (M = 10%Ni-90%Co)/Al_2O_3, (d) 25%M (M = 25%Ni-75%Co)/Al_2O_3, and (e) 25%M (M = 50%Ni-50%Co)/Al_2O_3. (Cyan) is reduction of Co_3O_4 to CoO, and (Green) CoO to Co^0.

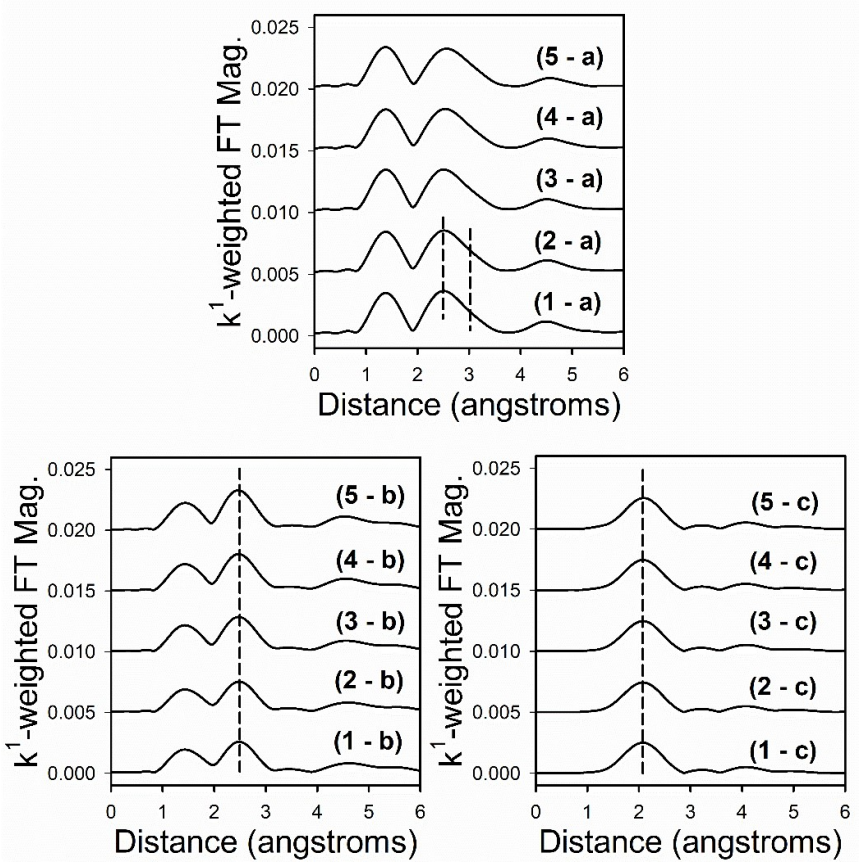

Figure 10: Co K-edge EXAFS spectra of (a) initial point consisting of primarily Co_3O_4, (b) point of maximum CoO content, and (c) final spectrum consisting of primarily Co^0 for (1) 25%Co/Al_2O_3, (2) 25%M (M = 2.5%Ni-97.5%Co)/Al_2O_3, (3) 25%M (M = 5%Ni-95%Co)/Al_2O_3, (4) 25%M (M = 10%Ni-90%Co)/Al_2O_3, (5) 25%M (M = 25%Ni-75%Co)/Al_2O_3, (6) 25%M (M = 50%Ni-50%Co)/Al_2O_3.

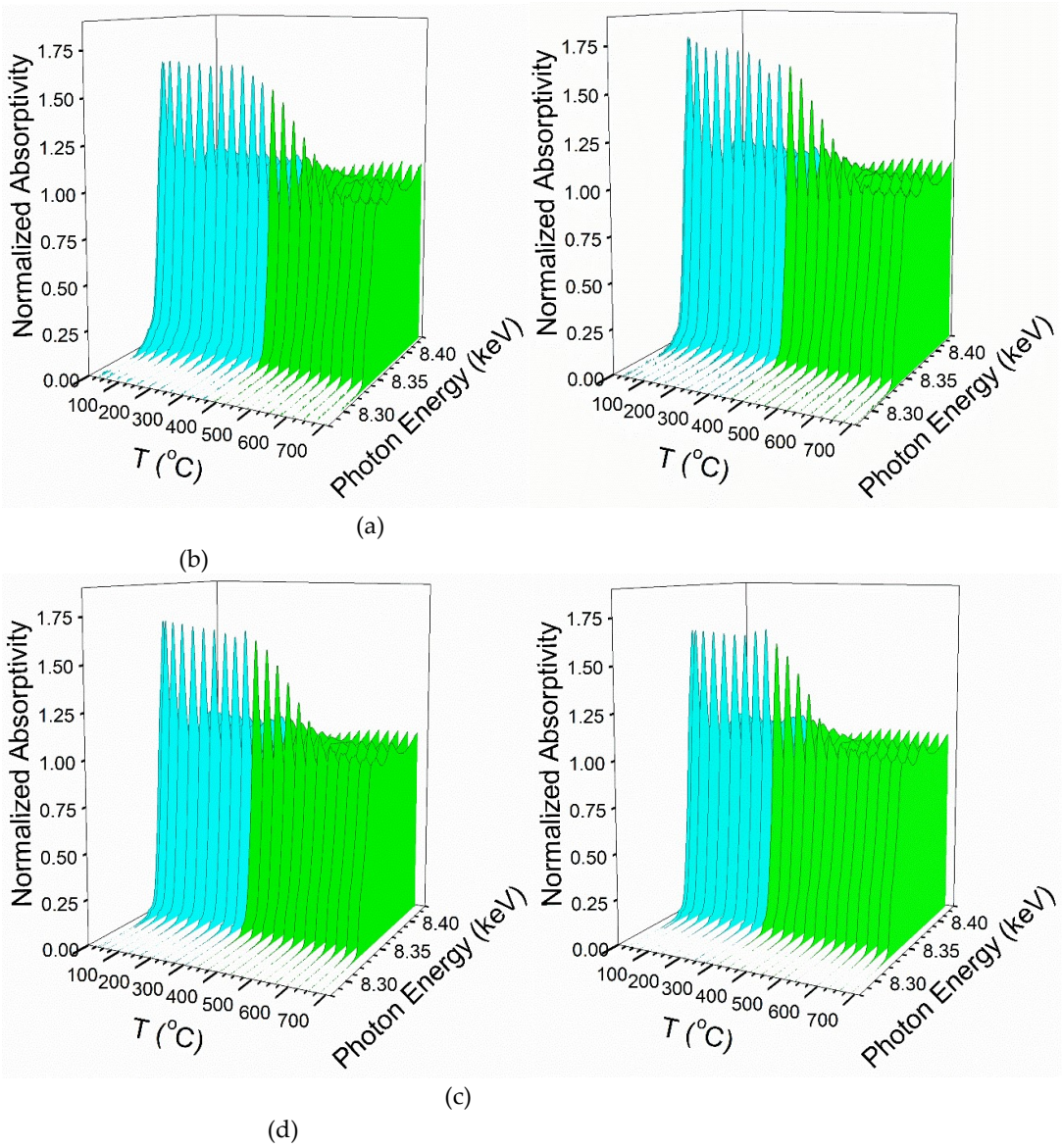

Figure 11: H_2-TPR-XANES spectra at the Ni K-edge of (a) 25%M (M = 5%Ni-95%Co)/Al_2O_3, (b) 25%M (M = 10%Ni-90%Co)/Al_2O_3, (c) 25%M (M = 25%Ni-75%Co)/Al_2O_3, and (d) 25%M (M = 50%Ni-50%Co)/Al_2O_3. (Cyan) is Ni^{2+} (e.g., NiO) associated with cobalt oxides during reduction of Co_3O_4 to CoO. (Green) is reduction of Ni^{2+} to Ni^0 when NiO reduction is associated with CoO reduction to Co^0.

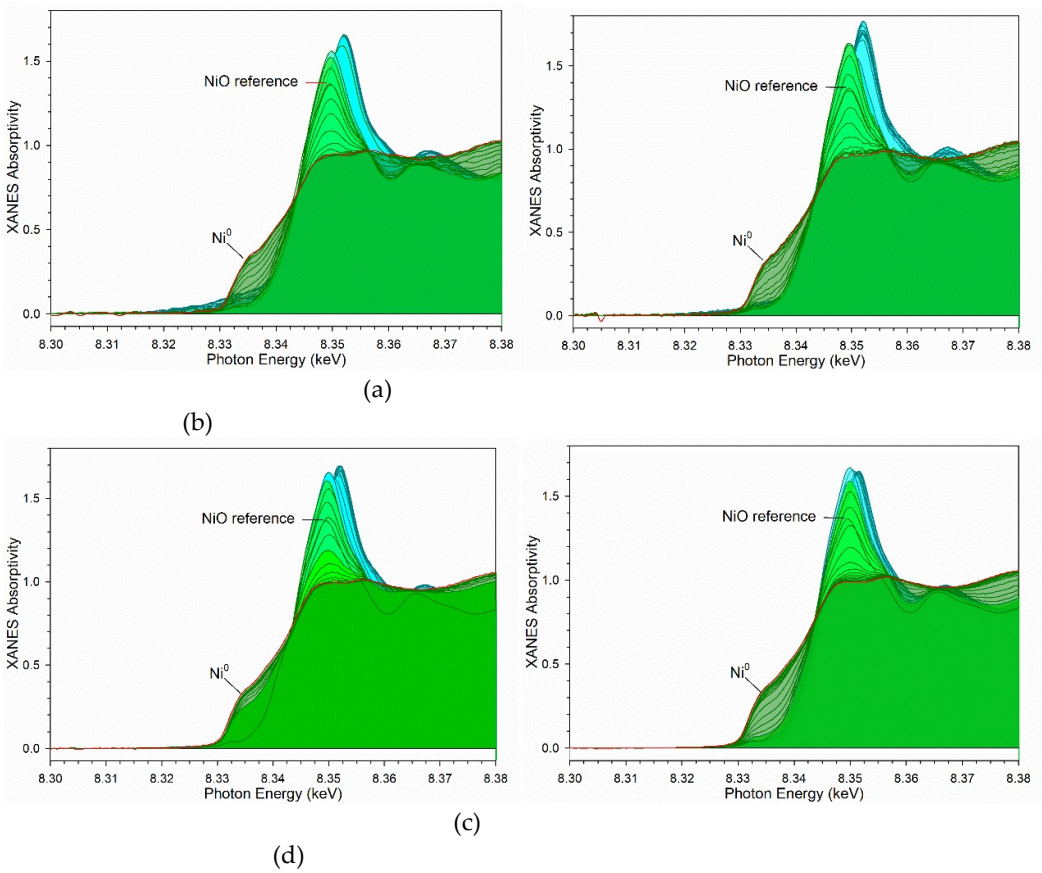

Figure 12: H_2-TPR-XANES spectra at the Ni K-edge of (a) 25%M (M = 5%Ni-95%Co)/Al_2O_3, (b) 25%M (M = 10%Ni-90%Co)/Al_2O_3, (c) 25%M (M = 25%Ni-75%Co)/Al_2O_3, and (d) 25%M (M = 50%Ni-50%Co)/Al_2O_3. (Cyan) is Ni^{2+} (e.g., NiO) associated with cobalt oxides during reduction of Co_3O_4 to CoO. (Green) is reduction of Ni^{2+} to Ni^0 when NiO reduction is associated with CoO reduction to Co^0.

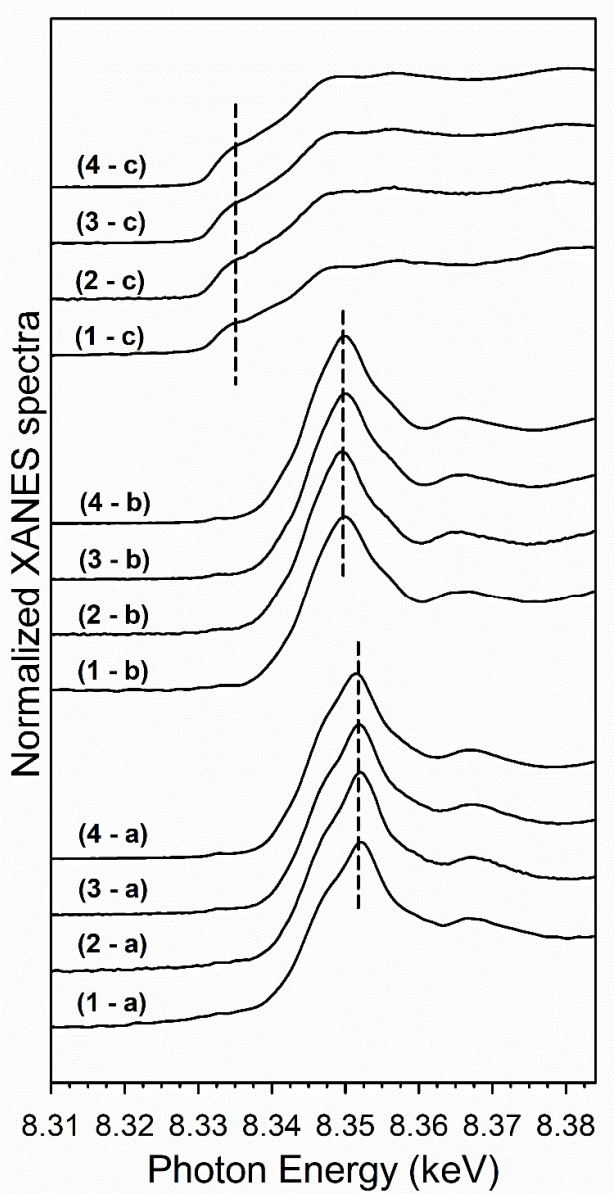

Figure 13: Ni K-edge XANES spectra of (a) initial point consisting of primarily NiO associated with Co_3O_4, (b) point consisting of primarily NiO associated with CoO, and (c) final spectrum consisting of primarily Ni^0 for (2) 25%M (M = 2.5%Ni-97.5%Co)/Al_2O_3, (3) 25%M (M = 5%Ni-95%Co)/Al_2O_3, (4) 25%M (M = 10%Ni-90%Co)/Al_2O_3, (5) 25%M (M = 25%Ni-75%Co)/Al_2O_3, (6) 25%M (M = 50%Ni-50%Co)/Al_2O_3.

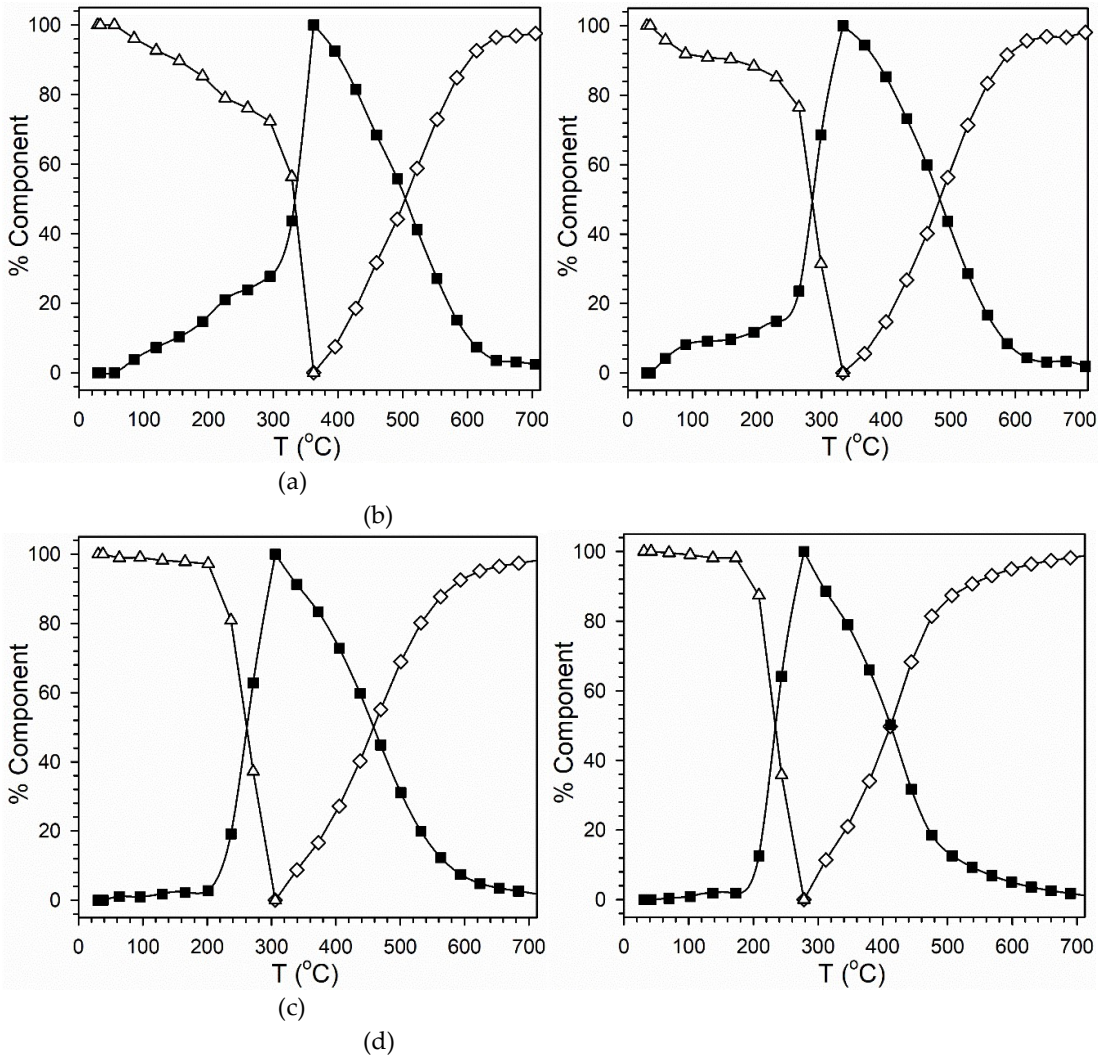

Figure 14: LC fittings of H_2-TPR-XANES spectra at the Ni K-edge of (a) 25%M (M = 5%Ni-95%Co)/Al_2O_3, (b) 25%M (M = 10%Ni-90%Co)/Al_2O_3, (c) 25%M (M = 25%Ni-75%Co)/Al_2O_3, and (d) 25%M (M = 50%Ni-50%Co)/Al_2O_3. Legend: △ Co_3O_4 associated with Ni^{2+}, ■ CoO associated with Ni^{2+}, and ◇ Ni^0 associated with Co^0.

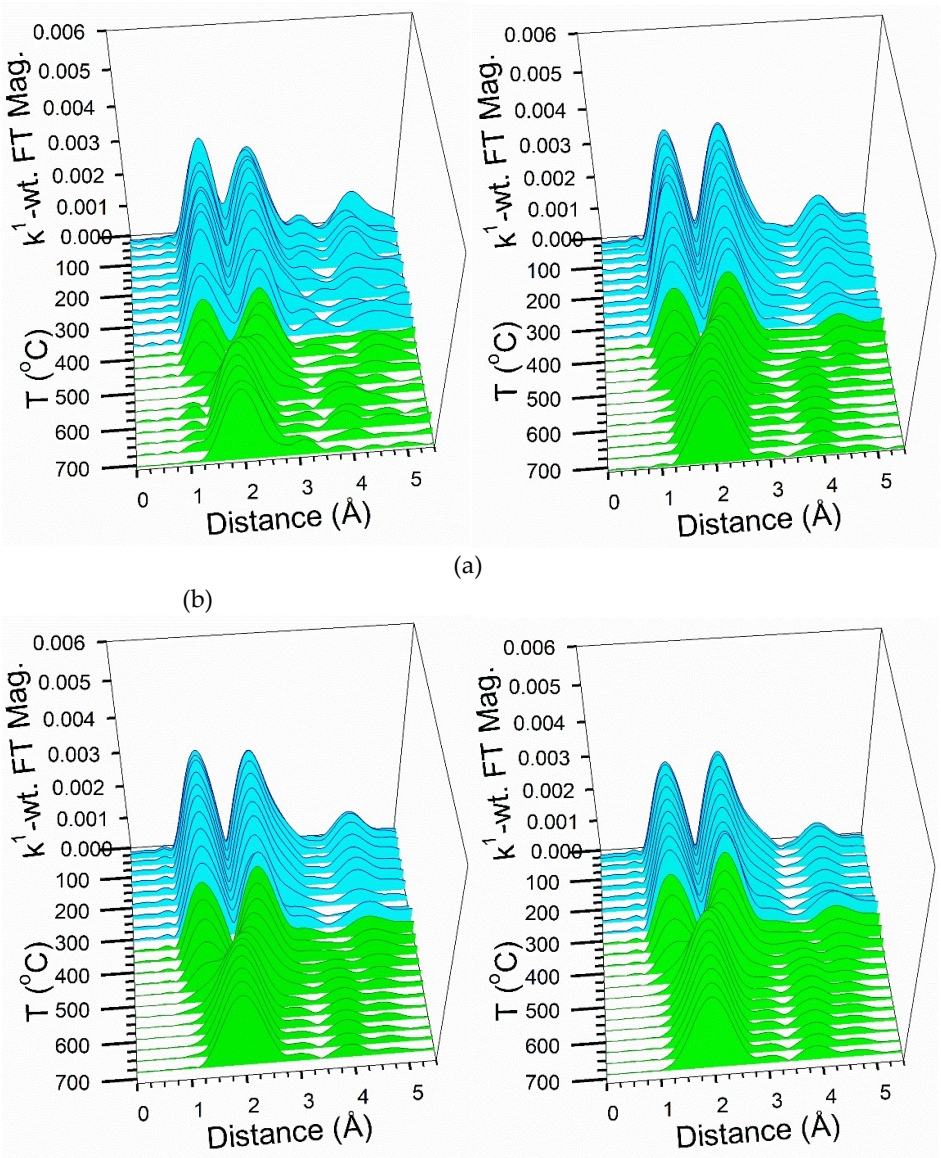

Figure 15: H_2-TPR-EXAFS spectra at the Ni K-edge of (a) 25%M (M = 5%Ni-95%Co)/Al_2O_3, (b) 25%M (M = 10%Ni-90%Co)/Al_2O_3, (c) 25%M (M = 25%Ni-75%Co)/Al_2O_3, and (d) 25%M (M = 50%Ni-50%Co)/Al_2O_3. (Cyan) is Ni^{2+} (e.g., NiO) associated with cobalt oxides during reduction of Co_3O_4 to CoO. (Green) is reduction of Ni^{2+} to Ni^0 when NiO reduction is associated with CoO reduction to Co^0.

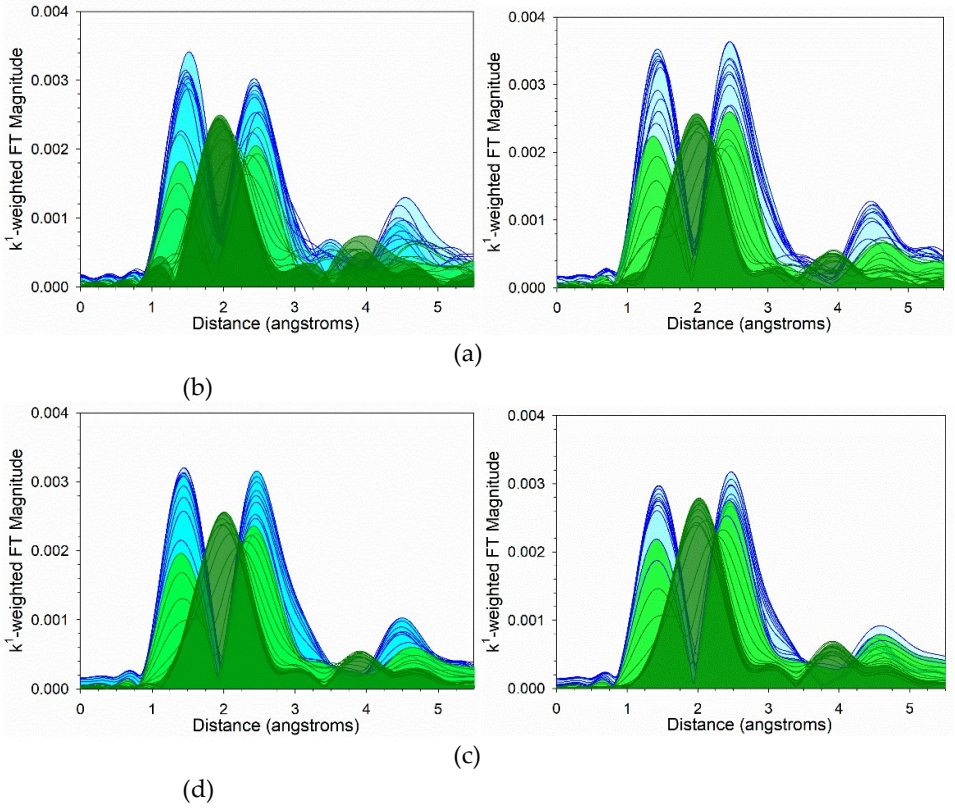

Figure 16: H_2-TPR-EXAFS spectra at the Ni K-edge of (a) 25%M (M = 5%Ni-95%Co)/Al_2O_3, (b) 25%M (M = 10%Ni-90%Co)/Al_2O_3, (c) 25%M (M = 25%Ni-75%Co)/Al_2O_3, and (d) 25%M (M = 50%Ni-50%Co)/Al_2O_3. (Cyan) is Ni^{2+} (e.g., NiO) associated with cobalt oxides during reduction of Co_3O_4 to CoO. (Green) is reduction of Ni^{2+} to Ni^0 when NiO reduction is associated with CoO reduction to Co^0.

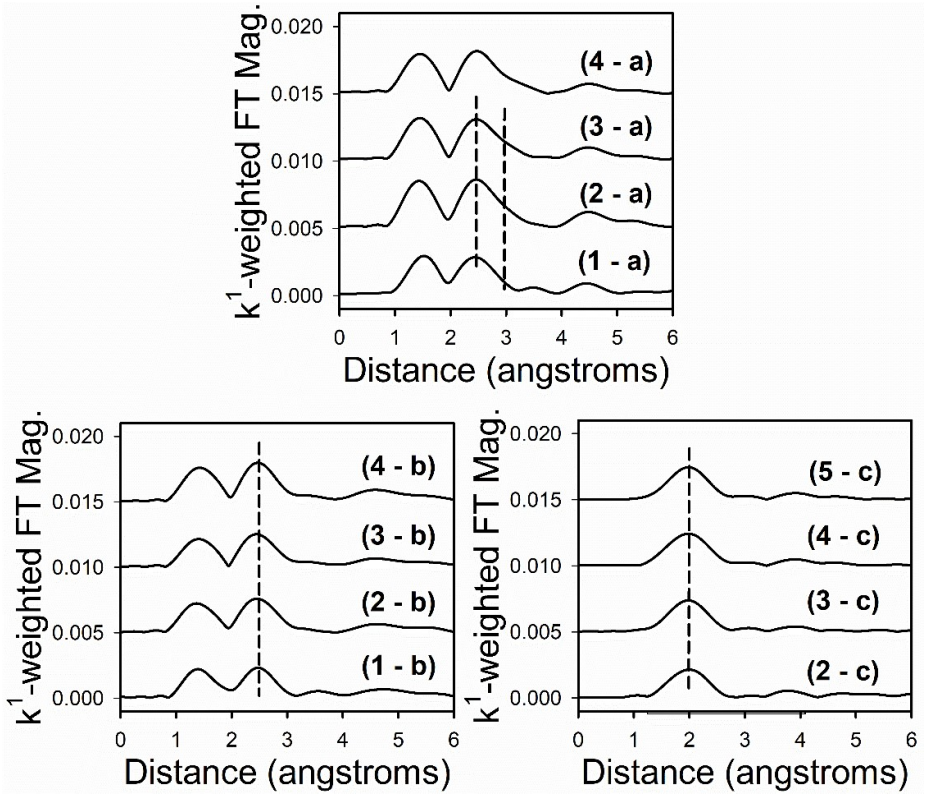

Figure 17: Ni K-edge EXAFS spectra of (a) initial point consisting of primarily NiO associated with Co_3O_4, (b) point consisting of primarily NiO associated with CoO, and (c) final spectrum consisting of primarily Ni^0 for (2) 25%M (M = 2.5%Ni-97.5%Co)/Al_2O_3, (3) 25%M (M = 5%Ni-95%Co)/Al_2O_3, (4) 25%M (M = 10%Ni-90%Co)/Al_2O_3, (5) 25%M (M = 25%Ni-75%Co)/Al_2O_3, (6) 25%M (M = 50%Ni-50%Co)/Al_2O_3.

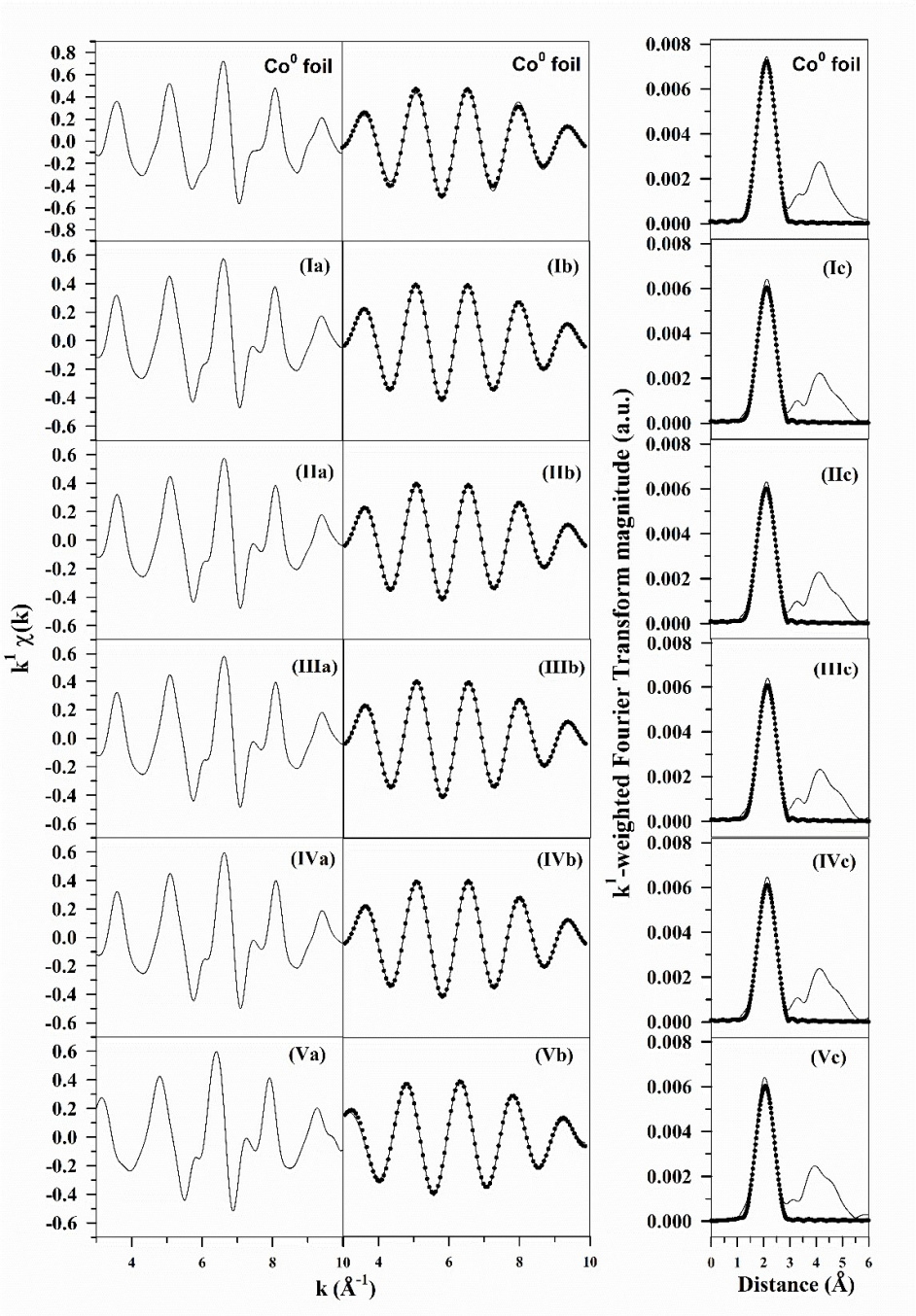

Figure 18: EXAFS fittings for Co K-edge data, including (a) raw k^1-weighted $\chi(k)$ data, (b) (solid line) filtered k^1-weighted $\chi(k)$ data and (filled circles) results of the fittings, and (c) (solid line) raw k^1-weighted Fourier transform magnitude and (d) (solid line) filtered k^1-weighted Fourier transform magnitude and (filled circles) results of the fittings for Co^0 foil, (I) 25%Co/Al_2O_3, (II) 25%M (M = 5%Ni-95%Co)/Al_2O_3, (III) 25%M (M = 10%Ni-90%Co)/Al_2O_3, (IV) 25%M (M = 25%Ni-75%Co)/Al_2O_3, (V) 25%M (M = 50%Ni-50%Co)/Al_2O_3.

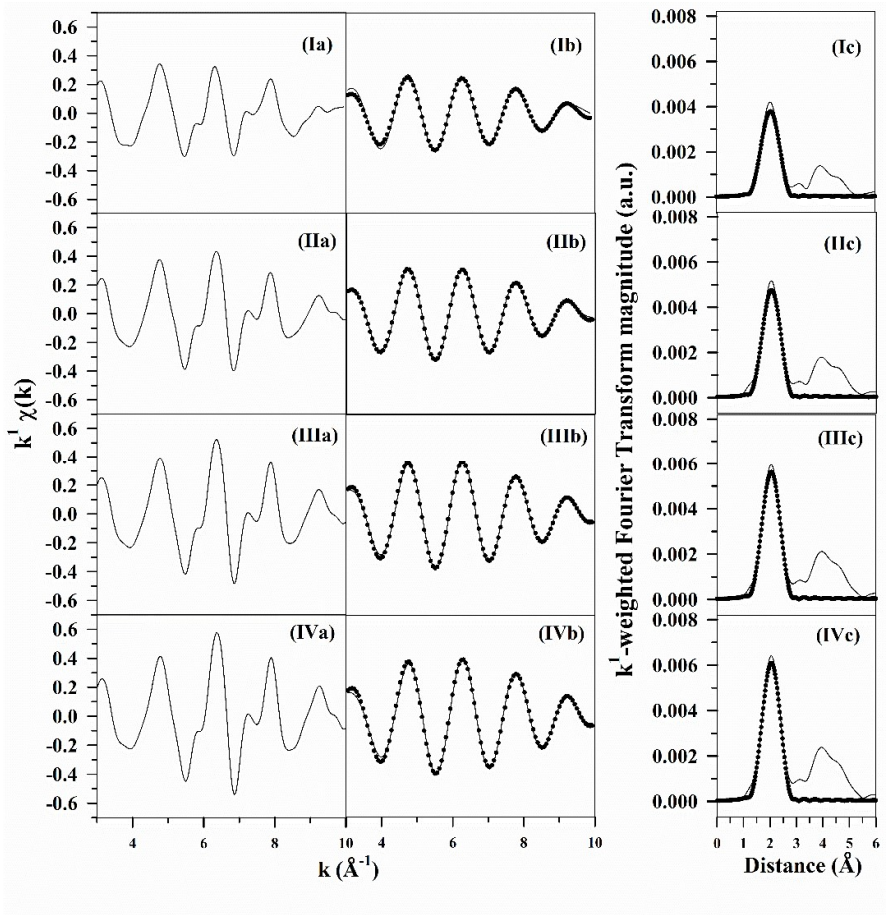

Figure 19: EXAFS fittings for Ni K-edge data, including (a) raw k^1-weighted $\chi(k)$ data, (b) (solid line) filtered k^1-weighted $\chi(k)$ data and (filled circles) results of the fittings, and (c) (solid line) raw k^1-weighted Fourier transform magnitude and (d) (solid line) filtered k^1-weighted Fourier transform magnitude and (filled circles) results of the fittings for (I) 25%M (M = 5%Ni-95%Co)/Al_2O_3, (II) 25%M (M = 10%Ni-90%Co)/Al_2O_3, (III) 25%M (M = 25%Ni-75%Co)/Al_2O_3, (IV) 25%M (M = 50%Ni-50%Co)/Al_2O_3.

Table 3: Results of EXAFS fitting* for data acquired near the Co and Ni K edges for catalysts following TPR-EXAFS after cooling. The fitting ranges were $\Delta k = 3 – 10$ Å^{-1} and $\Delta R = 1.2 – 2.8$ Å. *S_0^2 set to 0.90. Mixing parameter fixed to nominal value.

Sample Description	N Co-Co metal	R Co-Co (Å) metal	N Co-Ni metal	R Co-Ni (Å) metal	N Ni-Ni metal	R Ni-Ni (Å) metal	N Ni-Co metal	R Ni-Co (Å) Metal	e_0 (eV)	σ^2 (Å^2)	r-factor
100Co	9.9	2.489 (0.003)	-	-	-	-	-	-	6.37 (0.45)	0.00731 (0.00043)	0.0010
5Ni:95Co	9.9 (0.78)	2.489 (0.0053)	0.50 (0.04)	2.481 (0.0053)	0.32 (0.03)	2.472 (0.0053)	6.3 (0.59)	2.481 (0.0053)	6.32 (0.813)	0.00787 (0.00076)	0.014
10Ni:90Co	9.4 (0.48)	2.492 (0.0034)	0.94 (0.05)	2.483 (0.0034)	0.75 (0.04)	2.475 (0.0034)	7.5 (0.41)	2.483 (0.0034)	6.56 (0.527)	0.00777 (0.00048)	0.0035
25Ni:75Co	8.0 (0.31)	2.491 (0.0026)	2.0 (0.08)	2.482 (0.0026)	1.9 (0.08)	2.474 (0.0026)	7.4 (0.32)	2.482 (0.0026)	6.71 (0.401)	0.00719 (0.00036)	0.0023
50Ni:50Co	6.5 (0.36)	2.491 (0.0035)	3.3 (0.18)	2.483 (0.0035)	3.2 (0.18)	2.475 (0.0035)	6.4 (0.36)	2.483 (0.0035)	-4.39 (0.613)	0.00659 (0.00049)	0.0034

2.4 Catalytic activity

CO conversion in the first 200 h is shown in Figure 20. The CO conversion for the unpromoted catalyst has an initial value of 42.5%, then it slightly decreases in the first few hours until a steady-state value of 39.5% was reached. This trend is typical for cobalt-based catalysts. In contrast, CO conversion progressively increases for all nickel promoted catalysts. 5%Ni-95%Co and 10%Ni-90% exhibit similar CO conversion trends as the initial value is close to 20% and it continuously increases reaching 34%, whereas 25%Ni-75Co has a higher initial CO conversion (29%) and it reaches a steady-state value of 36%.

The evolution of selectivities (CH_4, CO_2, C_2-C_4 and C_{5+}) with T.o.S. is shown in Figure 21. CH_4 selectivity and C_{5+} selectivities are stable at 7.6% and 80.7%, respectively, for the unpromoted catalyst. The addition of nickel increases initial CH_4 selectivity, whereas it decreases initial C_{5+} selectivity. Fortunately, CH_4 selectivity for the nickel promoted catalyst slowly decreased with T.o.S. For example, the initial CH_4 selectivity for 25%M-25%Ni-75%Co is 13.4%, but it reaches 9.5% after 200 h. So, the difference as compared to Co/Al_2O_3 decreases from 5.8% (absolute) to just 1.9%.

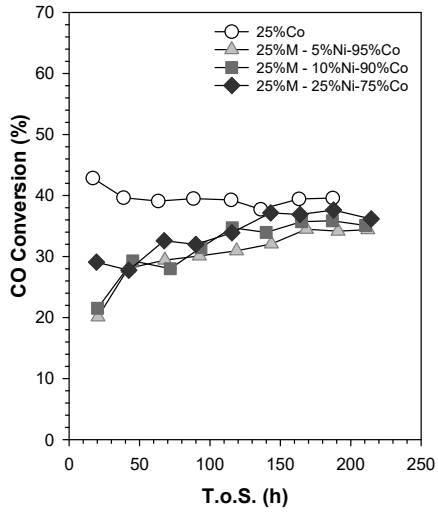

Figure 20: Evolution with T.o.S. of CO conversion for the prepared catalyst (process conditions: T = 220, H_2/CO = 2 mol/mol, P= 20.6 bar, S.V. = 3.4 slph per g_{cat})

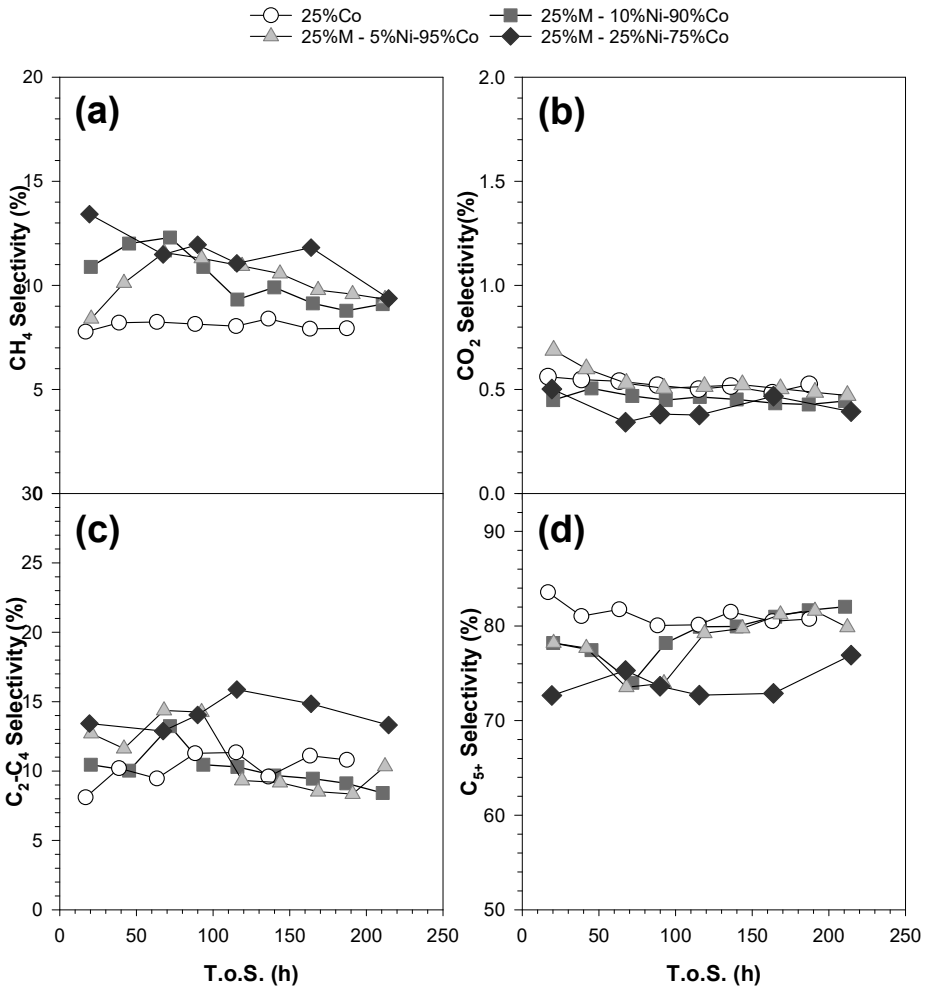

Figure 21: Evolution with T.o.S. of (a) CH_4 (b) CO_2 (c) C_2-C_4 and (d) C_{5+} selectivity for the prepared catalyst (process conditions: P= 20.6 bar, H_2/CO = 2 mol/mol, T = 220°C, S.V. = 3.4 slph per g_{cat}).

The olefin/parafin ratio for unpromoted and nickel promoted catalysts decreases with increasing carbon number starting with ethylene species and moving upward (Figure 22). This trend is typically observed for cobalt based catalysts. However, even if the trend with the carbon number is similar among the different catalysts, the olefin content decreases by increasing the nickel content. Indeed, the olefin/parafin ratio for C_3 species is 2.5 for 25%Co, while it is only 1 for the 25%M- 75%Co-25%Ni. At higher carbon number the difference among the different Ni/Co loadings is not so pronounced because of the tendency of olefins to readsorb on active sites [24]. The high hydrogenation capability of nickel promoted samples is also observed by a slight decrease in chain growth probability. Indeed $\alpha_{c5\text{-}c16}$ slightly decreases from 0.85 for 25%Co to 0.83 for 25%M-25%Ni-75%Co.

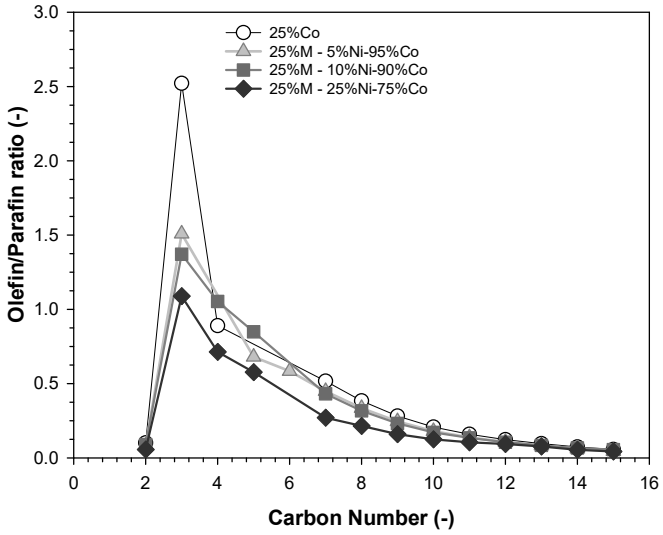

Figure 22: Olefin/Parafin ratio at T.o.S. ~150 h (process conditions: P= 20.6 bar, H_2/CO = 2 mol/mol, T = 220°C, S.V. = 3.4 slph per g_{cat}).

3. Discussion

The promotion of nickel on cobalt-based catalyst does not significantly influence the morphological properties, as all the samples have similar surface area (~92 m^2/g), pore volume and pore diameter. The effect of nickel on the structural properties was investigated by XRD and STEM. XRD patterns for all the calcined catalysts showed the typical peaks associated with Co_3O_4, while no diffraction peaks associated with NiO or Ni^0 were observed suggesting that a mixed metal oxide was formed. Intimate contact between cobalt and nickel was also confirmed by elemental mapping during STEM analysis, as well as by comparing TPR-XANES profiles at nickel and cobalt K-edges. Initially, nickel is associated with Co_3O_4, and then it undergoes a change in the electronic structure to a form of nickel associated with CoO. Further evidence for solid solution formation is that the Ni^{2+} associated with Co_3O_4 (Ni K-edge results) and the Co_3O_4 reduce over a similar temperature range, such that the temperatures at 50% conversion match very well, especially at higher Ni/Co ratios.

TPR-XANES and hydrogen chemisorption/O_2 titration show that nickel has a beneficial effect on cobalt reducibility. The reduction of cobalt oxide is shifted to lower temperature with increasing Ni/Co ratio, and the percentage of metal reduction is increased. Voss et al. [19] have observed an improvement in the reducibility when nickel was added as the first reduction step shifts significantly to lower temperature with increasing the nickel loading. The authors proposed a hydrogen spillover from the nickel sites to cobalt oxide sites. However, the previous observed similarities in temperatures ranges between Co_3O_4 to CoO and Ni^{2+}-Co_3O_4 to Ni^{2+}-CoO as well as the second reduction step to the metallic phase during TPR-XANES, suggests that maybe not only H_2 spillover is involved, but rather that a chemical effect exists in leading to the formation of Co-Ni alloy.

Cobalt-based catalysts are usually characterized by deactivation in the first few days. The possible mechanisms for this deactivation are: re-oxidation of small metallic cobalt cluster to inactive CoO_x, sintering, some carbon deposition or solid-state reaction between cobalt and support [4, 25, 26]. Thermodynamic calculations clearly show that when the cobalt crystallites have a diameter lower than 4.4 nm, they may be re-oxidized in the steam/hydrogen environments of FTS [7, 8]. This initial decline and leveling off period for CO conversion typical of cobalt-based catalysts was not observed for the nickel promoted systems. Rytter et al. [18] have also observed an activation period in the first 40 h. They proposed a catalyst reconstruction in the first stage of operation where nickel and cobalt partially segregate, thereby exposing the cobalt clusters to FTS reaction. However,

additional investigations are needed to speculate the events occurring during this induction time. Interestingly, the performances of nickel promoted catalysts are stable, despite having lower cobalt loading than 25%Co/Al_2O_3. This suggests that nickel can stabilize cobalt metal nanoparticles. Rytter et al. [18] further proposed that the higher stability for Co-Ni alloys could be due to the suppression of the carbon deposition and by suppressing re-oxidation phenomena via H_2 spillover.

Addition of nickel has changed the product distribution. In particular, the initial methane selectivity increases by increasing the nickel loading, whereas the initial C_{5+} selectivity decreases. Higher CH_4 selectivities were also observed in previous works, where different Ni/Co ratios were studied [10, 16, 18]. Interestingly, the selectivities of Co/Ni catalysts improve with time on-stream to nearly match those of pure Co catalysts. Furthermore, the olefin content decreases as well as the chain growth probability by increasing the Ni/Co ratio. These results are not surprising because of the high hydrogenation capability of nickel. Furthermore, Ishihara at al. [12] studying Co-Ni alloys supported on SiO_2 found that cobalt electronically interacts with nickel in the outer shell orbitals by creating adsorption sites having a new electron density. These new sites have the highest H adsorption strengths. Thus, hydrogen competes more effectively in the adsorption sites in co-adsorption of CO and H_2 for Co-Ni alloy relative to pure cobalt based catalyst.

Finally, it is interesting to compare the activity/$ (Table 4) as nickel and cobalt have different market prices. The price of cobalt is reported to be 2.13 times the price of nickel. Thus, the partial substitution of cobalt with nickel would be an advantage in terms of total catalyst cost. At steady state conditions the activity/$ for the 25%M-25%Ni-75%Co is best among the nickel promoted and unpromoted catalyst; also, at that point, the selectivities nearly match those of the pure Co based catalysts.

Table 4: Activity/$ at steady-state condition for the tested catalyst.

Sample ID	Activity/$
25%Co	39.5
25%M – 5%Ni-95%Co	35.4
25%M – 10%Ni-90%Co	36.8
25%M – 25%Ni-75%Co	41.9

4. Materials and Methods

4.1 Catalyst preparation

The conventional slurry impregnation method was used to prepare the catalyst containing 25% metal by weight, with the following Ni/Co atomic ratios: 0/100, 5/95, 10/90, 25/75 and 50/50. The support was Catalox 150 γ-alumina with a surface area of 150 m^2/g. Nickel nitrate and cobalt nitrate (Alfa Aesar) served as the precursors to load the nickel and cobalt together (i.e., in a single solution) onto the γ-Al_2O_3 support. In this method, the ratio of the weight of alumina to the volume of solution used was 1:1 as reported in a Sasol patent [1], , such that loading solution prepared was approximately 2.5 times the pore volume.. The total metal loading was added by two impregnation steps with 12.5 % of metal by weight for each step. Between each step, the catalyst was dried at 60 °C under vacuum in a rotary evaporator, then the temperature was slowly increased until 100 °C. After the second impregnation, the catalyst was dried and then calcined in flowing air for 4 h at 350 °C.

4.2 Characterization

A Micromeritics 3-Flex system (Norcross, GA, USA) using N_2 (UHP N_2, Airgas, Lexington, KY) for physisorption was used to measure BET surface area and porosity properties. Before testing, the samples were pre-treated at 160 °C and 50 mTorr for at least 12 h. The BJH method was employed to calculate the average pore volume and pore diameter.

XRD spectra were collected with a Philips X'Pert diffractometer with monochromatic Cu Kα radiation (λ=1.54Å). The conditions employed included a scan rate of 0.01° per step, 2θ range of 10-90, and a scan time of 4 s per step.

Prior to STEM characterization, the samples were pre-treated in hydrogen (American Welding & Gas, Lexington, KY, USA) at 350°C for 18 h, cooled down to room temperature and then passivated with a mixture of 1%O_2 in nitrogen (American Welding & Gas, Lexington, KY, USA). STEM analysis was performed with an FEI Talos F200X instrument (Thermo Scientific, Waltham, MA, U.S.A.) equipped with BF, DF2, DF4 and HAADF detectors. The imaging was collected with a field emission gun using an accelerating voltage of 200 kV and a high speed Ceta 16M camera, while Velox software(Thermo Scientific, Waltham, MA, U.S.A.) was used for data processing. The samples were dispersed in ethanol (Alfa Aesar, Haverhill, MA, U.S.A.), sonicated, and then drop onto a carbon-coated copper grid and dried in air.

Hydrogen chemisorption and the following pulse re-oxidation was carried out using an Altamira AMI-300 unit (Altamira Instruments, Pittsburgh, PA, USA). The sample was reduced at 350°C (ramping rate at 2°C/min) for 10 h in 10 cm^3/min of UHP H_2 (Airgas, San Antonio, TX, USA) blended with 20 cm^3/min of UHP argon (Airgas, San Antonio, TX, USA). Then, the temperature was cooled to 100°C, and UHP argon (30 cm^3/min) was flowed through the catalytic bed to avoid the adsorption of weakly bound hydrogen. Next, the temperature was increased to 350°C at 10°C/min in flowing argon to desorb the chemisorbed hydrogen. The hydrogen peak obtained during the temperature programmed desorption was integrated and the moles of hydrogen evolved was determined by comparing to calibration pulses. Pulses of UHP O_2 (Airgas, San Antonio, TX, USA) were then passed through the reactor to re-oxidize the catalyst until saturation was achieved. The percentage of reduction was estimated with two different methods. In the first approach, nickel and cobalt metal were assumed to oxidize to NiO and Co_3O_4, respectively. However, in a second approach, we assumed all Co_3O_4 converted at least to CoO during the reduction, and that a fraction of NiO and CoO converted to Ni^0 and Co^0. Thus, during re-oxidation step, the Ni^0 and Co^0 is first oxidized to NiO and CoO. Then, all CoO oxidizes to Co_3O_4. These two approaches set minimum and maximum limits for the cobalt cluster size when the uncorrected dispersion is modified by considering the percentage of reduction by the metal, as follows:

% Dispersion (Uncorrected) = (# metal atoms on the surface)/(# metal atoms in the sample)
% Disp. (Corrected) = (# metal atoms on the surface)/[(# metal atoms in the sample)(% reduction)]

4.3 H_2-TPR XANES-EXAFS

In-situ H_2-TPR XAFS experiments were carried out at the Materials Research Collaborative Access Team (MR-CAT) beamline at the Advanced Photon Source, Argonne National Laboratory. A cryogenically cooled Si (1 1 1) monochromator selected the incident energy and a rhodium-coated mirror rejected higher order harmonics of the fundamental beam energy. The experiment setup was analogous to that outlined by Jacoby [27]. The in-situ TPR of 6 catalysts were performed in stainless-steel multi-sample holder (3.0 mm i.d. channels) Approximately 6 mg of each catalyst was loaded as a self-supporting wafer in each channel. The catalyst was diluted with alumina in a weight ratio of approximately 1:1. The holder was located in the center of a quartz tube, equipped with Kapton windows, thermocouple and gas ports and. The amount of catalyst loaded was optimized for the Co and Ni K edges, considering the absorption by aluminum of the Al_2O_3 . The quartz tube was positioned in a clamshell furnace mounted on the positioning table. Each sample cell was placed relative to the beam and the position of the table was adjusted to an accuracy of 20 μm (for repeated scans). Once the catalyst positions were fine-tuned, the reactor was purged with He (100 ml/min) for more than 5 min and then the reactant gas (a mixture H_2/He, 3.5%) was flowed through the samples (100 ml/min). The temperature was increased to 700°C (ramp of ~1.0 °C/min) and then held for 4 h. The Ni and Co K-edge spectra were collected in transmission mode. The Co metallic foil spectrum was also recorded simultaneously for energy calibration. X-ray absorption spectra for each catalyst were collected from 7500 to 9000 eV.

The WinXAS program was used to analyze the spectra collected during H_2-TPR EXAFS/XANES experiments [28]. Additional details of the EXAFS and XANES analyses for Co K-

edge data are reported in our previous work [29]. Ni K-edge data were processed in a similar manner (i.e., same Δk and ΔR in fittings). For qualitative comparisons of EXAFS and XANES results, the references used for Co^0, , CoO, and Co_3O_4 were the final spectrum, the point of maximum CoO content, and the initial spectrum of the TPR trajectory of undopped cobalt catalyst (25%Co/Al_2O_3). For Ni^0 and NiO, the references were NiO (Alfa Aesar, Puratronic, 99.998%, Tewksbury, MA, USA) and a Ni^0 foil.

For XANES analyses, linear combination fittings were carried out considering as reference compounds for Co K-edge data the initial spectrum (a mixture of Co^{3+} and Co^{2+} similar to Co_3O_4), the point of maximum CoO content, and the final spectrum after H_2 TPR (representing Co^0). At the Ni K-edge, the reference compounds were the first spectrum (Co_3O_4 associated with Ni^{2+}), the spectrum with highest CoO content associated with Ni^{2+}, and the final spectrum after H_2 TPR (representing ~100% Ni^0). The data reduction and fitting for EXAFS were performed using the catalysts in their final state following TPR and cooling in flowing H_2 using the WinXAS [28], Atoms [30], FEFFIT [31], and FEFF [31] programs. The k-range chosen for the fittings was 3-10 $Å^{-1}$. Fitting was confined to the first metallic coordination shell by applying a Hanning window in the Fourier transform magnitude spectra, and carrying out the back-transform to isolate that shell.

4.4 Reaction testing

Activity tests were performed in a 1 L continuously stirred tank reactor (CSTR) (PPI, Warminster, PA, USA). Additional information on the lab scale rig can be found elsewhere [32]. In a typical test, 9.6 g of catalyst (63 < dp < 125 μm) was loaded into a fixed bed reactor. The catalyst was reduced at 350°C for 20 h, feeding 30 Nl/h H_2/He mixture (1:3 v/v, American Welding & Gas, Lexington, KY, USA) at atmospheric pressure. The reduced catalyst was transferred by pneumatic transfer under the protection of inert gas to a CSTR containing 310 g of melted Polywax 3000 (Baker Petrolite, Houston, TX, USA). In situ reduction for the transferred catalyst was performed at atmospheric pressure and 230°C overnight feeding 30 Nl/h pure H_2 (American Welding & Gas, Lexington, KY, USA). In this work, the catalytic testing was carried out at the following process conditions:, P = 20.2 bar, T = 220°C, a stirring speed of 750 rpm and H_2/CO = 2 mol/mol. The unconverted reactants and the products leaving the CSTR were sent to a warm trap, in which the temperature was set at 100 °C, and then to a cold trap maintained at 0 °C. The uncondensed stream was reduced to atmospheric pressure, while the flowrate and the composition were measured by a wet test meter and by an online 3000A micro-GC (Agilent, Santa Clara, CA, USA), respectively. The micro-GC is equipped with four different columns (Plot U , Molecular Sieve, OV-1 and, Alumina) and TCD. The reaction products were collected in three traps maintained at different temperatures: a hot trap (200 °C), a warm trap (100 °C), and a cold trap (0 °C). The products were separated into different fractions (wax, oil, and aqueous) for quantification. The oil (C_4-C_{20}) fraction was analyzed with a 7890 GC (Agilent, Santa Clara, CA, USA) equipped with DB-5 (60 m x 0.32 mm x 0.25μm, Agilent J&W) column and FID, while waxes (C_{21}-C_{60}) were analyzed with an HP 6890 GC equipped with ZB-1HT column (30 m x 0.25 mm x 0.10 μm, Zebron) and FID.

5. Conclusions

Bimetallic catalysts with different Ni/Co ratios were prepared by standard aqueous incipient impregnation. N_2 adsorption/desorption results show that the addition of nickel has no effect on the morphological properties as similar surface area, pore volume and pore diameter are obtained independently from the Ni/Co ratio. XRD patterns of the samples have the peaks associated with Co_3O_4, whereas no diffraction peaks associated with Ni were observed. Thus, this suggests a Co-Ni solid oxide solution might be formed. STEM and TPR-XANES show the nickel and cobalt are in intimate contact, strongly suggesting the formation of a Co-Ni alloy. Moreover, TPR-XANES results indicate that nickel promotion improves the cobalt reducibility by systematically shifting the reduction profiles to lower temperatures. The similarities in temperature ranges between Co_3O_4 to CoO and Ni^{2+}-Co_3O_4 to Ni^{2+}-CoO, as well as the second reduction step to the metallic phase during

TPR-XANES, suggests that not only H_2 spillover is involved, but that a chemical effect is likely. This is due to intimate contact in the solid solution that leads to the formation of the Co-Ni alloy.

The catalyst performance during FTS, in terms of conversion, selectivity and stability, were evaluated using a CSTR. Nickel promoted catalysts have lower initial CO conversion, which progressively increases with T.o.S. until a steady-state value is achieved. This CO conversion trend is inverted as compared to the typical induction period observed for Co/Al_2O_3, where the activity progressively declines and levels off because of deactivation phenomena. The stability of the Co-Ni alloy may be due to the stabilization of metallic cobalt nanoparticles by nickel addition, resulting in robust nanoparticles even at lower cobalt content compared to commercial Co loadings. CH_4 selectivity increases by increasing nickel loading because of the higher hydrogenation capability of the Co-Ni alloy. However, the difference in CH_4 selectivity between the Ni-promoted and unpromoted catalyst (in terms of the absolute value) decreases with T.o.S., which is beneficial; in fact, after stabilization, the C5+ selectivities were quite similar between catalysts prepared with Co-Ni versus Co alone. Finally, the steady-state activity/$ for Ni/Co ratio of 25/75 is slightly higher than $25\%Co/Al_2O_3$.

Author Contributions: Conceptualization, catalyst preparation, catalyst characterization, formal analysis, writing, GJ. Catalyst preparation, catalyst characterization, formal analysis, SCK. Catalyst preparation, catalyst characterization, formal analysis, RC. Catalyst preparation, catalyst characterization, formal analysis. CDW Reaction testing, characterization, formal analysis, conceptualization, writing, MM. Project administration, resources, CLM. Catalyst preparation, supervision, resources, DCC. Catalyst characterization, data curation, resources, supervision, AJK. Formal analysis WDS.

Funding: Richard Garcia received funding from a UTSA College of Engineering Scholarship. His work was also supported by the USDA National Institute of Food and Agriculture, Interdisciplinary Hands-on Research Traineeship and Extension Experiential Learning in Bioenergy/Natural Resources/Economics/Rural project, U-GREAT (Undergraduate Research, Education and Training) program (2016-67032-24984). Caleb D. Watson acknowledges support from the Undergraduate NSF Research Program, supported by the National Science Foundation through Grant Award #1832388.

Acknowledgments: Argonne's research was supported in part by the U.S. Department of Energy (DOE), Office of Fossil Energy, National Energy Technology Laboratory (NETL). Advanced Photon Source was supported by the U.S. Department of Energy, Office of Science, Office of Basic Energy Sciences, under Contract No. DE-AC02-06CH11357. MRCAT operations are supported by the Department of Energy and the MRCAT member institutions. CAER research was supported by the Commonwealth of Kentucky. Richard Garcia would like to acknowledge funding from a UTSA College of Engineering Scholarship. His work was also supported by the USDA National Institute of Food and Agriculture, Interdisciplinary Hands-on Research Traineeship and Extension Experiential Learning in Bioenergy/Natural Resources/Economics/Rural project, U-GREAT (Undergraduate Research, Education and Training) program (2016-67032-24984). Caleb D. Watson would like to acknowledge support from the Undergraduate NSF Research Program, supported by the National Science Foundation through Grant Award #1832388. Gary Jacobs would like to thank UTSA and the State of Texas for financial support through startup funds.

Conflicts of Interest: The authors declare no conflict of interest.

References

[1] H. Schulz, Short history and present trends of Fischer–Tropsch synthesis, Applied Catalysis A: General, 186 (1999) 3-12.
[2] W.D. Shafer, M.K. Gnanamani, U.M. Graham, J. Yang, C.M. Masuku, G. Jacobs, B.H. Davis, Fischer–Tropsch: Product Selectivity–The Fingerprint of Synthetic Fuels, Catalysts, 9 (2019) 259.
[3] A.Y. Khodakov, W. Chu, P. Fongarland, Advances in the Development of Novel Cobalt Fischer–Tropsch Catalysts for Synthesis of Long-Chain Hydrocarbons and Clean Fuels, Chemical Reviews, 107 (2007) 1692-1744.
[4] H. Jahangiri, J. Bennett, P. Mahjoubi, K. Wilson, S. Gu, A review of advanced catalyst development for Fischer–Tropsch synthesis of hydrocarbons from biomass derived syn-gas, Catalysis Science & Technology, 4 (2014) 2210-2229.
[5] I. Glacier Resource Management Group, available online: http://www.infomine.com/investment).
[6] E. Iglesia, Design, synthesis, and use of cobalt-based Fischer-Tropsch synthesis catalysts, Applied Catalysis A: General, 161 (1997) 59-78.

[7] C. Hou, G. Xia, X. Sun, Y. Wu, C. Jin, Z. Yan, M. Li, Z. Hu, H. Nie, D. Li, Thermodynamics of oxidation of an alumina-supported cobalt catalyst by water in F-T synthesis, Catalysis Today, 264 (2016) 91-97.
[8] E. van Steen, M. Claeys, M.E. Dry, J. van de Loosdrecht, E.L. Viljoen, J.L. Visagie, Stability of Nanocrystals: Thermodynamic Analysis of Oxidation and Re-reduction of Cobalt in Water/Hydrogen Mixtures, The Journal of Physical Chemistry B, 109 (2005) 3575-3577.
[9] G. Jacobs, P.M. Patterson, T.K. Das, M. Luo, B.H. Davis, Fischer–Tropsch synthesis: effect of water on Co/Al2O3 catalysts and XAFS characterization of reoxidation phenomena, Applied Catalysis A: General, 270 (2004) 65-76.
[10] P. van Helden, F. Prinsloo, J.-A. van den Berg, B. Xaba, W. Erasmus, M. Claeys, J. van de Loosdrecht, Cobalt-nickel bimetallic Fischer-Tropsch catalysts: A combined theoretical and experimental approach, Catalysis Today, 342 (2020) 88-98.
[11] V. Shadravan, V.J. Bukas, G.T.K.K. Gunasooriya, J. Waleson, M. Drewery, J. Karibika, J. Jones, E. Kennedy, A. Adesina, J.K. Nørskov, M. Stockenhuber, Effect of Manganese on the Selective Catalytic Hydrogenation of COx in the Presence of Light Hydrocarbons Over Ni/Al2O3: An Experimental and Computational Study, ACS Catalysis, 10 (2020) 1535-1547.
[12] T. Ishihara, N. Horiuchi, T. Inoue, K. Eguchi, Y. Takita, H. Arai, Effect of alloying on CO hydrogenation activity over SiO2-supported Co◉Ni alloy catalysts, Journal of Catalysis, 136 (1992) 232-241.
[13] T. Ishihara, H. Iwakuni, K. Eguchi, H. Arai, Hydrogenation of carbon monoxide over the mixed catalysts composed of cobalt-nickel/manganese oxide-zirconium oxide and zeolite catalysts, Applied Catalysis, 75 (1991) 225-235.
[14] T. Ishihara, K. Eguchi, H. Arai, Hydrogenation of carbon monoxide over SiO2-supported Fe-Co, Co-Ni and Ni-Fe bimetallic catalysts, Applied Catalysis, 30 (1987) 225-238.
[15] Y. Sun, J. Wei, J.P. Zhang, G. Yang, Optimization using response surface methodology and kinetic study of Fischer–Tropsch synthesis using SiO2 supported bimetallic Co–Ni catalyst, Journal of Natural Gas Science and Engineering, 28 (2016) 173-183.
[16] K. Shimura, T. Miyazawa, T. Hanaoka, S. Hirata, Fischer–Tropsch synthesis over alumina supported bimetallic Co–Ni catalyst: Effect of impregnation sequence and solution, Journal of Molecular Catalysis A: Chemical, 407 (2015) 15-24.
[17] A. Eshraghi, A.A. Mirzaei, R. Rahimi, H. Atashi, Effect of Ni–Co morphology on kinetics for Fischer–Tropsch reaction in a fixed-bed reactor, Journal of the Taiwan Institute of Chemical Engineers, 105 (2019) 104-114.
[18] E. Rytter, T.H. Skagseth, S. Eri, A.O. Sjåstad, Cobalt Fischer−Tropsch Catalysts Using Nickel Promoter as a Rhenium Substitute to Suppress Deactivation, Industrial & Engineering Chemistry Research, 49 (2010) 4140-4148.
[19] G.J.B. Voss, J.B. Fløystad, A. Voronov, M. Rønning, The State of Nickel as Promotor in Cobalt Fischer–Tropsch Synthesis Catalysts, Topics in Catalysis, 58 (2015) 896-904.
[20] J. López-Tinoco, R. Mendoza-Cruz, L. Bazán-Díaz, S.C. Karuturi, M. Martinelli, D.C. Cronauer, A.J. Kropf, C.L. Marshall, G. Jacobs, The Preparation and Characterization of Co–Ni Nanoparticles and the Testing of a Heterogenized Co–Ni/Alumina Catalyst for CO Hydrogenation, Catalysts, 10 (2019) 18.
[21] P. Nikparsa, A.A. Mirzaei, R. Rauch, Modification of Co/Al2O3 Fischer–Tropsch Nanocatalysts by Adding Ni: A Kinetic Approach, International Journal of Chemical Kinetics, 48 (2016) 131-143.
[22] H. Yu, A. Zhao, H. Zhang, W. Ying, D. Fang, Bimetallic Catalyst of Co and Ni for Fischer-Tropsch Synthesis Supported on Alumina, Energy Sources, Part A: Recovery, Utilization, and Environmental Effects, 37 (2015) 47-54.
[23] G. Jacobs, W. Ma, P. Gao, B. Todic, T. Bhatelia, D.B. Bukur, B.H. Davis, The application of synchrotron methods in characterizing iron and cobalt Fischer–Tropsch synthesis catalysts, Catalysis Today, 214 (2013) 100-139.
[24] G.P. Van Der Laan, A.A.C.M. Beenackers, Kinetics and Selectivity of the Fischer–Tropsch Synthesis: A Literature Review, Catalysis Reviews, 41 (1999) 255-318.
[25] N.E. Tsakoumis, M. Rønning, Ø. Borg, E. Rytter, A. Holmen, Deactivation of cobalt based Fischer–Tropsch catalysts: A review, Catalysis Today, 154 (2010) 162-182.
[26] G. Jacobs, P.M. Patterson, Y. Zhang, T. Das, J. Li, B.H. Davis, Fischer–Tropsch synthesis: deactivation of noble metal-promoted Co/Al2O3 catalysts, Applied Catalysis A: General, 233 (2002) 215-226.
[27] M. Jacoby, X-RAY ABSORPTION SPECTROSCOPY, Chemical & Engineering News Archive, 79 (2001) 33-38.
[28] T. Ressler, WinXAS: a Program for X-ray Absorption Spectroscopy Data Analysis under MS-Windows, Journal of Synchrotron Radiation, 5 (1998) 118-122.
[29] G. Jacobs, Y. Ji, B.H. Davis, D. Cronauer, A.J. Kropf, C.L. Marshall, Fischer–Tropsch synthesis: Temperature programmed EXAFS/XANES investigation of the influence of support type, cobalt loading, and noble metal

promoter addition to the reduction behavior of cobalt oxide particles, Applied Catalysis A: General, 333 (2007) 177-191.
[30] B. Ravel, ATOMS: crystallography for the X-ray absorption spectroscopist, Journal of Synchrotron Radiation, 8 (2001) 314-316.
[31] M. Newville, B. Ravel, D. Haskel, J.J. Rehr, E.A. Stern, Y. Yacoby, Analysis of multiple-scattering XAFS data using theoretical standards, Physica B: Condensed Matter, 208-209 (1995) 154-156.
[32] G. Jacobs, M.C. Ribeiro, W. Ma, Y. Ji, S. Khalid, P.T.A. Sumodjo, B.H. Davis, Group 11 (Cu, Ag, Au) promotion of 15%Co/Al2O3 Fischer–Tropsch synthesis catalysts, Applied Catalysis A: General, 361 (2009) 137-151.